Flood risk assessment in Ténès city (Algeria) using land cover based on machine learning methods and Pléiades tri-stereo images

Zaabar Narimane, Niculescu Simona, Mihoubi Mustapha Kamel

Flood risk assessment in Ténès city (Algeria) using land cover based on machine learning methods and Pléiades tri-stereo images

Zaabar Narimane[1,2*], Niculescu Simona[1,3], Mihoubi Mustapha Kamel[2]

[1] University of Western Brittany, CNRS, LETG Brest UMR 6554 CNRS, Brest, France, and Laboratoire Mobilisation et Valorisation des Ressources en Eau (MVRE), Ecole Nationale Supérieure d'Hydraulique (ENSH), Blida, Algeria, 3109000, Zaabar.nari@gmail.com.

[1] University of Western Brittany, CNRS, LETG Brest UMR 6554 CNRS, Brest, France, Simona.Niculescu@univ-brest.fr.

[3]Institut Universitaire Français (IUF)

[2] Laboratoire Mobilisation et Valorisation des Ressources en Eau (MVRE), Ecole Nationale Supérieure d'Hydraulique (ENSH), Blida, Algeria, 3109000, mihkam@ensh.dz.

*Corresponding author

Abstract

On a global scale, a considerable amount of life, property, and resources are lost because of the increasing frequency and severity of flooding occurrences. This necessitates the development of worldwide, thorough flood risk assessments and urbanization policies. This work used sophisticated remote sensing data hydraulic models to create an effective and appropriate methodology to flood risk assessment in a coastal city located in in western Algeria. In the first stage, Sentinel-2 optical data was classified using deep learning and machine learning methods for land cover and land use (LULC). The CNN deep model based on LULC was selected because of its outstanding overall accuracy. Then, a 1-D HEC-RAS hydraulic model was performed, integrating LULC maps with a higher precision, topography using a digital surface model (DSM) derived from Pléiades tri-stereo data, and another digital elevation model (12 meters). Flood hydrographs were as well constructed for four scenarios (10, 20, 50, and 100 years) using hydrometric data. The 1D flood mode was indeed validated using a flood event data. Flood hazard, LULC and flood risk maps were derived. Results show the high flood hazard areas are concentrated on the left bank of the Oued Allala river and urban cities near to the coast. According to the results of the flood hazard simulation of 100 years, built-up areas and roads are the LULC classes most affected by flood hazard, with more than 94.4% and 69.34 % for DSM tri-stereo and DEM models, respectively. As well, results of flood risk assessment by combining hazard risk and LULC vulnerability show that for the DSM model, 0.48%, 44.55%,

and 53.11%, and 54.04% of flooded areas are in low, medium, and high flood risk, respectively. For the DEM model, 3.14%, 45%, and 51.04% of flooded areas are in low, medium, and high flood risk, respectively. Results confirmed that topographic resolution of models and LULC accuracy of CNN models can highly affect hydraulic simulation output results. Based on the obtained results, Ténès city needs necessary planning for flood risk management, particularly in the coastal area. Derived maps can serve as valuable information for regional and national decision-making.

Keywords: flood risk, flood-prone area, LULC, machine and deep learning, hydraulic model, vulnerability, flood scenarios, Pléiades tri-stereo.

1. Introduction

Floods are becoming more frequent and severe worldwide, resulting in significant losses in terms of people, property, and resources. The International Disaster Database Emergency Events Database (EM-DAT project) estimates that since 2020, floods have affected over 5,000 persons worldwide, with approximate increases of +2 percentage points in the economic damage caused by floods as a share of global GDP. Consequently, effective planning for flood-prone regions and conducting hydraulic analyses are crucial components in reducing and managing flood risks (Kumar and Singh, 2024; Nguyen and Kim, 2023; Garcia and Liu, 2022; Smith and Thompson, 2022). In Algeria, various environmental and socioeconomic factors contribute to flood risk. The occupation of flood-prone areas has become a pressing issue, as many Algerian cities have developed around springs and rivers, particularly in coastal regions. Unfortunately, as urban development encroaches on these flood zones, vulnerability to flooding increases. This situation necessitates careful temporal and spatial consideration in the implementation of policies for effective planning and flood risk management (Bornane et al., 2019; Goumrasa et al., 2021; Boutaghane et al., 2022; Mokhtari et al., 2023).

Hydraulic and hydrological models, including conceptual, empirical, probabilistic, and physically based models, are employed for flood forecasting. These models have been developed over decades using field data and river observations. However, they face limitations due to insufficient data, lack of long-term observations, and difficulties accessing flood-prone areas. As well, unidimensional one-dimensional or two-dimensional hydraulic models, such as HEC-RAS (Hydrologic Engineering Centers River Analysis System) require precise spatial delineation of land use and land cover (LULC) in flood-prone areas, along with accurate topographical data (Psomiadis et al., 2021; Soliman et al., 2022; Phyo, 2023).

To address these challenges, remote sensing has emerged as a powerful tool for flood risk assessment and floodplain mapping in recent decades. High and very high spatial resolution (HSR and VHSR) satellite imagery provides essential data for delineating floodplains and assessing socio-economic damage and risk (Schumann et al., 2015; Domeneghetti, 2019; Munawar et al., 2022). The integration of remote sensing with hydraulic models offers unprecedented opportunities to simulate water depths and flood hazard characteristics, enhancing the spatial representation of floods. Remote sensing data significantly improves these models by providing timely and accurate information on LULC, topography, and hydrological conditions.

Literally, LULC maps serve as critical input data for hydraulic models, aiding in understanding how various surfaces—such as urban areas, forests, wetlands, and agricultural lands—interact with rainfall and runoff processes. As well, LULC accuracy has a strong impact on modeling quality (Lu et al., 2023; Natarajan et al., 2020 ; Yalcin, 2020). The classification of LULC through satellite data, machine learning and deep learning techniques has gained significant traction in the scientific community. Traditional machine learning algorithms, including support vector machines (SVM) (Nandam and Patel, 2021), random forests, (Adugna et al., 2022; Niculescu et al., 2020; Zaabar et al., 2021) and decision trees, remain vital for LULC classification. These methods are often combined with deep learning techniques to improve classification performance and interpretability. Deep learning models, particularly convolutional neural networks (CNNs), have become foundational for LULC classification, excelling in processing high-dimensional data like satellite imagery and automatically extracting features essential with distinguishing different LULC types (Bhosle and Musande, 2019; Kattenborn et al., 2021; Zaabar et al., 2022).

Among the recent developments of deep learning in the field of LULC using Machine and Deep Learning we recall: Remote sensing image classification using an ensemble framework without multiple classifiers (Dou et al., 2024); Scene classification of high-resolution remotely sensed images based on ResNet (Wang et al., 2019); Large-scale land use/land cover extraction from Landsat OLI images using feature relationships matrix based deep-shallow learning (Dou et al., 2024); Crop type mapping in the central part of the North China Plain using Sentinel-2 time series and machine learning (Luo et al., 2023).

In (Lu et al., 2023) study, the authors emphasized the LULC Classification using UAV Remote Sensing through Transformer–CNN Hybrid models. Integrated features in the proposed method considered both global and local context pieces of information. Three deep learning models,

including DE-UNet and DE-UN, were tested on UAV images and achieved the highest LULC classification accuracy. In similar, (Wang et al., 2023) presented a new extraction framework for land cover characterization in mining areas based on deep MFE-ResNet model. The method was combined with an object-based approach applied on Gaofen-2 satellite. The model was compared with six other deep learning methods and analysed for accuracy in two several study areas of varying sizes from two different perspectives. According to results in this work, mining areas information were well acquired and this confirms the contribution of these deep models to challenge such issues.

Therefore, the effectiveness of LULC usage hinges on the quality of the classification produced. Accordingly, land cover data can serve as input for hydraulic models, running or be utilized as post-processed information to evaluate the flood vulnerability of each land cover class.

Solaimani et al., (2024) explored in the present study, the capability of Random Forest (RF) and Support Vector Machine (SVM) algorithms investigated in combination with Sentinel series and Landsat-8 images to prepare the 2019 flood map. Then, the flood hazard map of these areas was prepared using the new hybrid Fuzzy Best Worse Model-Weighted Multi-Criteria Analysis (FBWM-WMCA) model. Results of the study showed effective flood output maps with the best accuracy of LULC input maps.

(Phyo, 2023) proposed an efficient method of flood inundation by HEC-RAS modelling and GIS mapping for disaster risk management. The authors emphasized using remote sensing input data such as land use, land cover, soil type, curve number, and differences in analytical simulation utilizing 1D and 2D to enhance the body of work. For classifying the dam size, the ICOLD Large Dams Classification and USACE Embankment Size Classification Criteria were used because they match Myanmar's condition for hazard potential and inflow design flood. This research investigates the potential impacts of climate change on flood frequency and intensity in Algeria, providing a framework for future risk assessments.

In similar, Digital elevation models (DEMs) are essential for analyzing flood hazard and conducting risk assessments. They play a significant role in accurately depicting river geometries and floodplains, which can affect hydraulic flood simulations and the extent of simulated flood events. Recent advancements in optical and radar satellite sensors have enabled the acquisition of highly precise DEMs, which are frequently utilized in hydraulic modeling studies (Annis et al., 2020; Casas et al., 2006; Das et Lindenschmidt., 2021; Ettritch et al., 2018; Fathy et al., 2019; Lamichhane et Sharma., 2018; Mihu-Pintilie et al., 2019). These studies

predominantly employ models derived from light detection and ranging (LIDAR), the Shuttle Radar Topography Mission (SRTM), the Advanced Spaceborne Thermal Emission and Reflection Radiometer (ASTER; Tuia et al., 2011), the Canadian Digital Elevation Model (CDEM), unmanned aerial vehicles (UAVs), and the Advanced Land Observing Satellite (ALOS; Zhang et al., 2019).

Recently, the emergence of stereoscopic satellite systems has further improved the capabilities of remote sensing sensors, allowing for the generation of digital elevation models from stereoscopic optical images. The Pléiades system, in particular, offers high-resolution Digital Surface Models (DSM) of complex terrains due to its ability to capture up to three images of the same area with stereo angles ranging from 6° to 28° (Bagnardi et al., 2016; Lacroix et al., 2015). Despite their potential, these models are rarely taken advantage for hydraulic flood modelling due to their recent introduction and specific acquisition conditions. For instance, Bennani et al. (2019) assessed flood risk in a semi-arid region of Morocco using topographic data from Pléiades tri-stereo, demonstrating that these models are suitable for hydraulic simulations and provide valuable opportunities for flood risk mapping in complex areas. The recent availability of high-resolution elevation data allows for the implementation of hydraulic simulation approaches across various catchments, facilitating the creation of accurate floodplain maps.

The main objective of this study is to employ a comprehensive, synergistic approach to analyze the flood risk of the Oued Allala River, which flows through the coastal city of Ténès in western Algeria. This analysis integrates remote sensing techniques with hydraulic simulations. Two topographic models, the DSM from Pléiades stereo and the DEM model, were acquired to construct the river and floodplain geometries, which were then compared. LULC used classifications were derived from previous research conducted by the authors, utilizing Sentinel-2 images processed through deep learning and machine learning models. Hydraulic simulations were executed using the HEC-RAS model and the most accurate LULC classification, and the accuracy of the modelling outcomes were validated against surveyed data from a flood event that occurred in 2017. Subsequently, hazard, vulnerability, and flood risk maps were generated based on the outputs of the hydraulic modelling.

2. Study area

The study area is located in northern Algeria, midway between Algiers and Oran along the Mediterranean coast (Figure 1). The region is influenced by the Mediterranean climate and is characterized by a warm, temperate climate with high rainfall during the winter months.

The city, on the one hand, plays an important regional role due to its geographical location and its current and future facilities. According to a study by the *Agence Nationale de Gestion Intégrée des Ressources en Eau* (AGIRE), the population is expected to reach 50,000 by 2029. The urban areas mobilized to meet the needs of this population are increasingly developing, and they are mobilized around the urban center of Ténès to meet the needs of this population.

In recent years (November 2001, November 2011, and November 2012), the city of Ténès has experienced flooding in its lower zone. Homes and infrastructure have been damaged, and sometimes lives have been lost. The most critical area corresponds to the coastal urban sector of the region. It includes small plains and adjacent hills around the confluence of the Oued Allala and Boufessousa rivers. These floods have developed due to the size of the watersheds and forest massifs, which aggravate forest fires and make it difficult to transport sediments and vegetation. The runoff from this drainage channel crosses a plain that narrows to about 900 meters before being discharged into the sea. In addition, seawater rises at the mouth of the river, preventing the floodwaters from draining properly. Furthermore, due to its regional importance, geographical location, and high risk of natural disasters, this study area was selected as part of the National Flood Control Strategy.

Therefore, in this study, the Oued Allala watershed was selected for the application of the proposed methodology. The Allala Basin includes the city of Ténès and its coastal area. It is located between 36.30° and 36.55° N latitude and between 1.05° and 1.45° E longitude, south of Ténès. The total area of the watershed is 307 km², and the main river of the watershed is 35 km long. The region has a maximum and minimum elevation between 1,032 and 44 m, respectively, and includes Ténès. It is a tourist city, a port city, and the second-largest city in the Wilaya of Chlef.

The region has a Mediterranean climate characterized by warm and temperate weather, with heavy rain in the winter. The average temperature is 18.6 °C, and the average total annual rainfall is about 585 mm (Kastali et al., 2021). The Allala watershed has a variety of landscapes, including urban areas, forests, and agricultural lands. The northern part of the basin is covered with pine forests. Annual crops such as cereals cover the southern part of the basin. This

diversity of land use categories requires a thorough understanding and identification of the landscape elements that are at risk of flooding in the area.

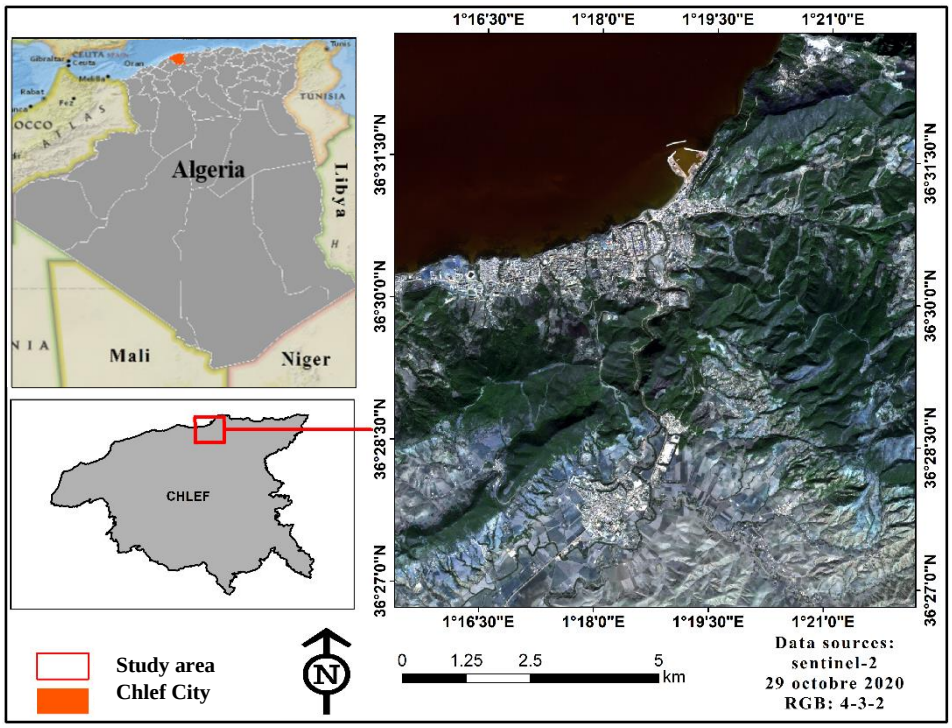

Figure 1. Location of the study site

3. Materials and methods

The workflow of the proposed method consisted of the following steps: (1) data collection and preprocessing, (2) land cover classification and validation using the proposed convolutional neural networks (CNN) model combined with object-based image analysis (OBIA), (3) hydraulic model construction, (4) model calibration and simulation, and (5) flood hazard and vulnerability map generation. Figure 2 shows a flowchart of the developed methods.

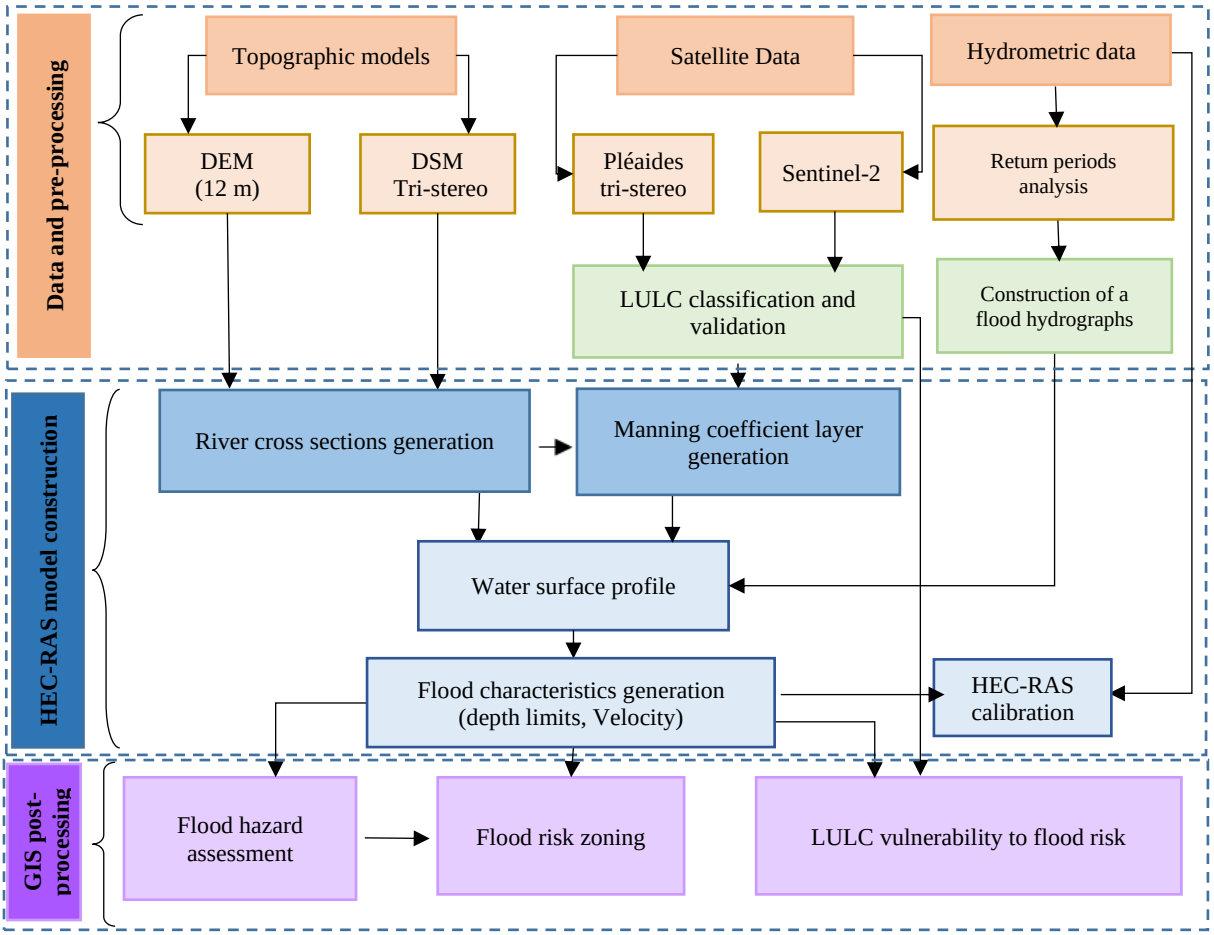

Figure 2. Flowchart of the proposed methodology

3.1. Data and preprocessing

3.1.1. Remote sensing data

- **Sentinel-2 data**

For the detailed delineation LULC of the Allala watershed, remote sensing data with different spatial resolutions were obtained. The data consists of a single Sentinel-2 at Level 2A image, atmospherically corrected. The Sentinel-2A image was acquired free of charge via the ESA platform (https://scihub.copernicus.eu/) on March 8, 2020. This image has 13 spectral bands and a high spatial resolution ranging from 10 to 60 m. The high spatial, spectral, and temporal resolution of Sentinel-2 satellites makes them well suited for LULC monitoring programs due to their high revisit frequency (10 days for a single Sentinel-2 satellite and 5 days for the combined constellation). Sentinel-2 band were then resampling to obtain a single resolution (10 m). Detailed specifications of Sentinel-2 image are described in table 1.

Table 1. Provided additional acquisition properties of Sentinel-2 imagery.

Data	band	Wavelength (nm)	Spatial Resolution (m)
Sentinel 2A Acquired on March 8, 2020	2	492.4	10
	3	559.8	
	4	664.6	
	8	832.8	
	5	704.1	20
	6	740.5	
	7	782.8	
	8a	864.7	
	11	1613.7	
	12	2202.4	
	1	442.7	60
	9	945.1	
	10	1373.5	

- **Topographic data**

The main objective of using topographic models in this research was to create our proposed hydraulic model to delineate flooded areas and flood characteristics. A comparison of DSM tri-stereo and DEM-12 m spatial resolution models was carried out in order to evaluate the effect of accurate urban topography on the hydraulic simulation procedure.

The DSM was extracted from the stereoscopic tri-image Pléiades with a very high spatial resolution. With its constellation and two satellites flying in sun-synchronous orbits with an inclination of 98.2° and an offset of 180°, the Pléiades system is the first of its kind to acquire at least three near-synchronous images of the same region at stereo angles varying between 6° and 28°. This stereoscopic capability makes it possible to generate accurate THRS-based DSMs for complex topographic surfaces (Lacroix et al., 2015). A single tri-stereoscopic Pléaides image covering the Allala watershed was acquired on October 22, 2022.

3.1.2. Hydrometric data

All hydraulic simulation calculations were performed using a hydrometric series of maximum daily flow discharges from the Sidi Akkacha hydrometric station over a 45-year period from 1972 to 2017, thanks to the presence of a hydrometric station monitoring the Oued Allala

watershed. The hydrometric data are provided by the Agence Nationale des Ressources Hydriques (ANRH). However, since data from the hydrometric station are not updated after 2017, we were able to obtain flow data up to 2017 within the parameters of this study and in light of national policy. Homogeneity tests were then performed to verify the independence and identical distribution of the chronic observations. In this sense, Wilcoxon (Kosiorowski et al., 2019), independence (Wald and Wolfowiz, 1943), and stationarity homogeneity tests were applied to the studied series of flows. In addition, according to the type of flooding that characterizes northern Algeria and, in particular, the studied region, multiple probability adjustment laws were tested on a series of maximum instantaneous flows. The adjustment law chosen to determine the quantiles corresponding to the return periods is the one best suited to the hydrological dataset. According to the results of the probability distribution, the flood hydrograph was constructed for four return periods (10, 25, 50, and 100 years).

3.2. Integrated land cover derived for the CNN model and HEC-RAS model for flood hazard assessment

3.2.1. LULC classification based on machine learning models

Previously derived LULC maps (Zaabar et al., 2021) were used as an indispensable database for the hydraulic simulation step, mainly to assess the impact on flood vulnerability. Machine and deep learning models were performed to LULC classifications. In the current proposed methodology, the derived classification with the highest overall accuracy index (OA) more than 92.2 % value was employed. It involves LULC classification using integrated method based on object-level image (OBIA) and CNN algorithm applied on Sentinel-2 image. LULC categories were identified using visual analysis and interpretation of the Pléiades VHSR image, producing eight predominant classes: water, barren land, buildings, agricultural land, non-agricultural land, roads, medium vegetation, and forest. Sample generation was split into two categories: training and test samples. The generation provided two vector datasets: training vector, which applied during the classification process; whereas the test vector was used in both accuracy assessments. CNN is a deep learning model technique designed for image classification. A representative CNN architecture consists of sequential layers (e.g., convolutional, pooling, and fully connected layers) and interconnected output layers using nonlinear operations (Wang et al., 2018). CNN architecture was created in Trimble eCognition Developer v.10 software (*eCognition*, 2021). The main layers characterizing CNN structural design implemented were the hidden, convolution, pooling, and fully connected layers; whereas the process consisted of

three main steps: creation of sample patches; generation of and training the model; and model application (figure 3).

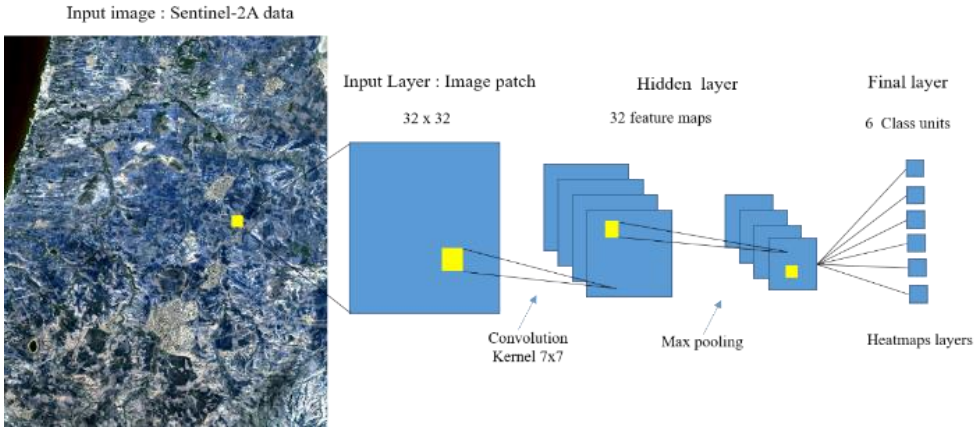

Figure 3. CNN architecture of Sentinel-2A image (Zaabar et al., 2022)

Based on training vector data represent classes, a 10000 32x32 pixels samples patches were created for predefined LULC classes. Two hidden layers, applied with max pooling and two kernel parameters of 7 and 3, respectively, were used to create and train the CNN architecture. Eight heatmaps are then created used as input of OBIA classification of LULC for the whole satellite image (figure 4).

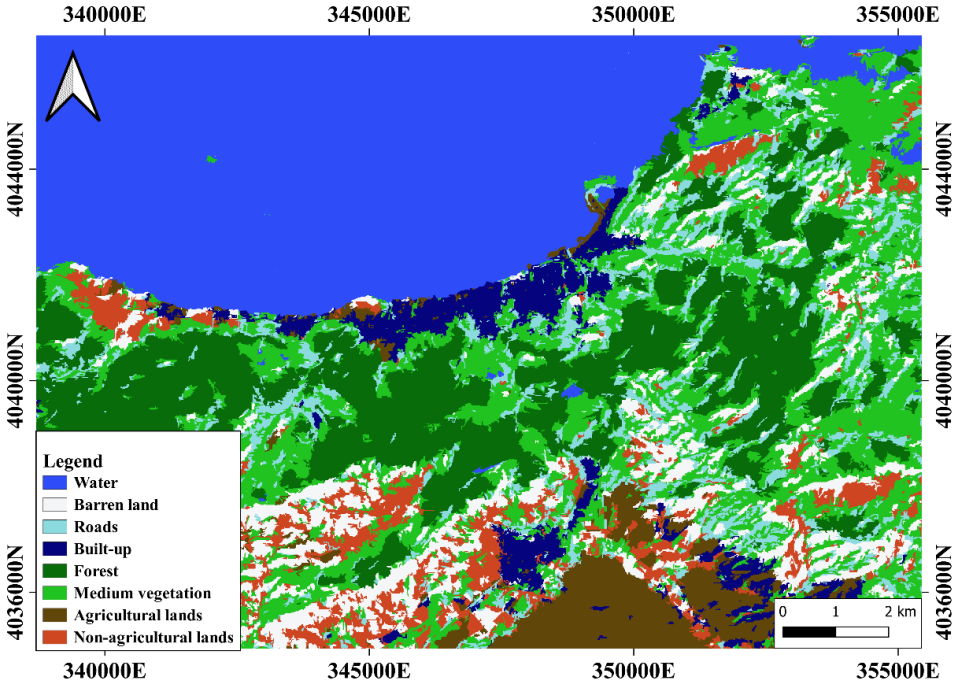

Figure 4. LULC classification performed with CNN model.

The LULC map was used as input layer in HEC-RAS model to generate layers of Manning roughness coefficient layer. Manning values, which determine surface roughness, were assigned according to different LULC categories, as classified by Sentinel-2 data. The appropriate determination of Manning values takes into account the presence of construction, bare areas, and agricultural or vegetated areas to provide a more realistic simulation of flood flow generation.

3.2.2. Topographic model generation

The hydraulic modelling process requires as input a DEM or DSM models that allows the representation of watercourses and floodplains. The DSM is generated from a tri-stereo image with a very high spatial resolution (less than 2 m), which allows the detection of vegetation cover, building rooftops, bare soil, and ground when nothing else is above it. A comparative study of DSM tri-stereo and DEM-12 m spatial resolution models was recommended to assess the impact of the accuracy of the urban topography on the hydraulic simulation process. The Pléiades system can acquire images in stereo tuples, often a pair or triplet, with n ranging from 2 to 25. Each image is then captured at a different angle of incidence and azimuth. In order to calculate the DSM, it is essential to consider all or part of the generated image. Therefore, images are acquired from different angles for the same area of interest. The generation of DSMs is often performed by different commercial software packages for processing stereoscopic satellite images (e.g., PCI Geomatica, ERDAS) or by open-source software developed by public institutions. In this work, DSMs were generated using the DataTerra on-demand DSM-OPT (*Digital Surface Models* from OPTical stereoscopic very-high-resolution imagery) service. This service was operated by the ForM@Ter (Solid Earth) cluster (www.poleterresolide.fr/le-service-dsm-opt/) in collaboration with the Theia (Continental Surfaces) cluster and the DINAMIS device. The MNS calculation takes into account terrain features, such as contrast, slope, and roughness, in the selection of radiometric image processing, the determination of image position, the correlation process, and the filtering of intermediate products. This is particularly useful for flood studies and simulations. In addition, we used this online tool to perform calculations based on the following parameters: landscape type: coastal; input images: the tri-stereo folder of acquired images containing images from different camera angles; area of interest: including the city of Ténès (northern part of the studied watershed); and DSM resolution factor: Here, a high factor was chosen to generate very high-resolution DSMs. The DSM and DEM topographic models used in the hydraulic simulation are shown in Figure 5.

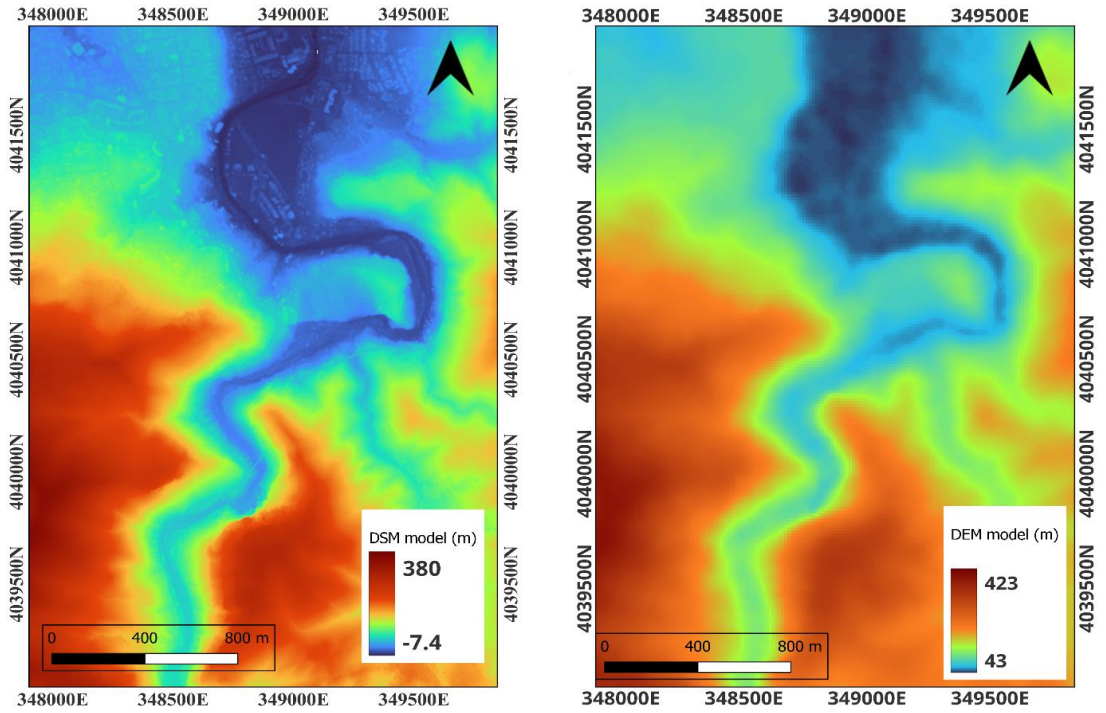

Figure 5. Overview of the Pléiades tri-stereo DSM (left) and DEM (right) models.

3.2.3. Creation and simulation of the hydraulic model

Based on the maximum flows corresponding to the return periods and their distribution probabilities, the simulation in this study was performed for four return periods: 10 years, 20 years, 50 years, and 100 years. For the downstream wave propagation, a one-dimensional mathematical flow integrated with the HEC-RAS model was used. This model is highly recommended for flood simulations, mainly in habergeon areas. It is easy to determine the energy equation in both time and space. In addition, the HEC-RAS model generates hydraulic characteristics with optimal numerical stability, such as flood limits, water depth, and wave propagation speed. In addition, the geometry of the plain was created using imported topographic data, including three essential components: the central line of the main channel, the limits of the minor bed of the main channel (main channel banks), the limits of the major bed (flow path), and cross-sections (*cross-sections*). Furthermore, the land cover raster file was integrated into the model using the *Terrain-add land cover map* tool available in RAS Mapper. A Manning roughness coefficient layer was created from this file by assigning roughness values to each land cover class.

Once the geometry is created (Figure 6), it can be opened and visualized using the geometric data module, which displays the cross-sections generated and the Manning layer assignment for all sections. In addition, the hydraulic simulation model was designed using the steady flow data tool. In the case of this study, the steady flow model was selected. At this stage, water

profiles were created corresponding to the four return periods analyzed in the study. The creation of water profiles using models such as HEC-RAS requires specifications on upstream and downstream boundary conditions. These specifications mainly include critical heads and normal slopes.

Hydraulic simulation using the steady flow analysis tool allows the modeling of flow profiles in fluvial, torrential, or mixed flow regimes for different simultaneous flows (USACE, 2016). At the start of the calculation, different characteristic layers were generated for each simulated water profile. The simulation results in HEC-RAS are used to generate hazard and vulnerability maps and flood risk assessments. These analyses are described in detail in the following sections, followed by model calibration, which is an essential step in confirming the reliability of the generated model.

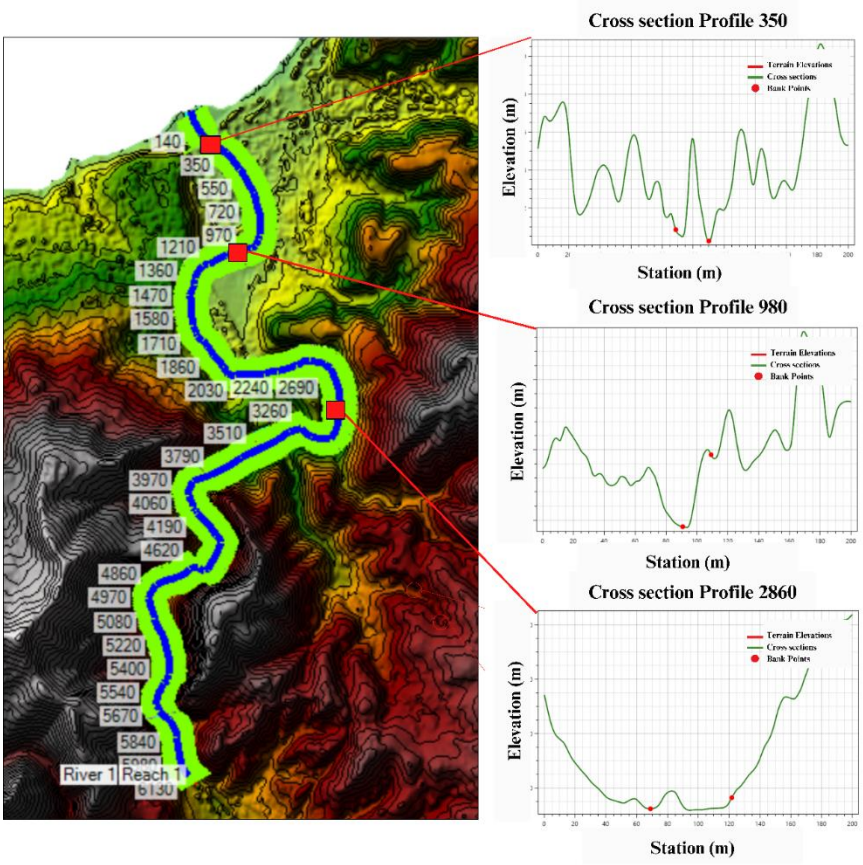

Figure 6. Layout and cross-sections of the main channel created by HEC-RAS.

3.2.4. Hydraulic model validation

The models were calibrated with a flood that occurred in 2017 and by varying the values of Manning's roughness coefficient, supported by a comparison of the simulated waterline with the observed one. The values assigned to the roughness coefficient for each land cover class are shown in Table 2.

Table 2. Calibrated Manning roughness coefficient values as a function of land-use classes.

LULC class	Water	Built-up	Roads	Barren land	Agricultural lands	Non-agricultural lands	Forest	Medium vegetation
Manning coefficient	0.30	0.025	0.013	0.035	0.035	0.035	0.2	0.2

3.3. Flood risk assessment

Risk is defined in terms of its two components: "hazard" and "vulnerability." Consequently, vulnerability is assessed by running the model based on the presence or absence of flooding in a given land use class. Based on the depth and velocity generated by the HEC-RAS calculation code and on the data provided by the land use maps, a spatial model was used to assess the risk with these two components, with the necessary processing carried out with HEC-RAS and the customized graphics module interface through a geographic information system (GIS) environment.

3.3.1. Flood hazard analysis

Hydraulic and hydrological parameters often define the hazard aspect of flood risk. Flood frequency is considered a widely accepted indicator for estimating flood risk. In fact, water depth is a critical parameter in quantifying flood risk and damage potential. The hazard level can thus be defined by the combination of the two parameters (i.e., flood depth and flow velocity; Kreibich et al. 2009; Psomiadis et al. 2021). This implies that the same flood event will affect a particular area with the same hydraulic characteristics, regardless of the land cover or land use component.

In this sense, several damage assessment criteria for flood risk have been developed, such as those proposed by the American Society of Civil Engineers (ASCE) and the US Bureau of Reclamation (USBR) In this study, the criteria proposed by the National Flood Risk Advisory Group (NFRAG) Committee (Smith et al., 2014) were reviewed and considered because, in a specific floodplain management study or emergency management analysis, there may be a clear need to use specific thresholds based on depth (h) and flow velocity (V). However, in a preliminary risk assessment or as part of a constraint analysis, there is also a recognized need for a combined set of hazard vulnerability curves that can be used as a general classification of flood risk in a floodplain. These combined flood hazard curves establish hazard thresholds that relate to the community's vulnerability to extreme events. The combined curves are divided into six hazard classifications that relate to specific vulnerability thresholds (Table 3). The

analytical application of this criterion was carried out in HEC-RAS using specific tools to calculate the quantity: depth x flow velocity. In addition, the classification according to the thresholds defined by this criterion was performed using an algorithm that we imported into HEC-RAS.

Table 3. Hazard Curves, Vulnerability Threshold, and Classification Limits (Smith et al., 2014).

Classification Limit (m^2/s)	**Descriptions**	**Hazard Vulnerability Classification**
≤ 0.3	Generally safe for vehicles, people, and building	H1
≤ 0.6	Unsafe for small vehicles	H2
≤ 0.6	Unsafe for vehicles, children, and older adults	H3
≤ 1.0	Unsafe for vehicles and people	H4
≤ 4.0	Unsafe for vehicles and people. All buildings vulnerable to structural damage	H5
> 4.0	Unsafe for vehicles and people All buildings vulnerable to failure	H6

These hazard classes have been reclassified into three classes for flood risk zoning: low-medium: h*v <0.6 m²/s, medium: 0.6 m²/s <h*v < 1 m²/s, and high - very high: h*v > 1 m²/s.

3.3.2. Flood vulnerability analysis

A variety of characteristics influences flood vulnerability. In this study, only land cover and land use are considered. In other words, floods with the same probability of exceeding the standard will have different levels of damage depending on land use characteristics and the level of damage. Vulnerability analysis, therefore, refers to the identification of land cover and land use areas that are likely to be affected by flooding during a given return period. Therefore, hazard maps were created by delineating flood zones on land cover and land use maps, and polygon files were used to define flood boundaries for each simulated return period. This describes the vulnerability aspect of a specific area to flood risk whether flooding will occur during the specified return period. The land cover and land use areas affected by each flood were reclassified to determine the total area at risk.

3.3.3. Flood risk analysis

Flood risk analysis combines the results of the vulnerability analysis and the hazard analysis. It is defined based on the relationship between the land cover and land use hazard categories and the flood depth and velocity hazard categories for a given area. In addition, the flood hazard

maps created as part of the risk analysis are compared to the land cover and land use hazard maps. The resulting attribute table is reclassified to establish the relationship between the two risk types. The analysis therefore represents the full flood risk potential for the affected land use, land cover categories, and flood hazard categories.

4. Results

In this section, we present the results of applying a 1D hydraulic model that integrates spatial data, mainly LULC maps, and topographic data from surface and hydraulic models to map flood-prone areas and assess global risk. Flood zone mapping and flood risk assessment are carried out for four return periods: 10 years, 20 years, 50 years, and 100 years, using the HEC-RAS model. The results described here mainly include frequency analysis, hydraulic simulation, and the results of hydraulic flood parameters, hazard analysis, and vulnerability analysis of land use classes to flood risk.

4.1. Flood frequency analysis and flood hydrographs

The flood hydrograph was constructed from the results of calculating maximum flows using the appropriate law for the hydrometric series and the time of concentration of the Oued Allala watershed. As a result, the value T_c = 8 hours was selected to calculate the base and flood times and then to construct the flood hydrograph for the six return periods using the Sokolovsky method (Figure 7). The maximum flows used for the hydraulic simulation with HEC-RAS are 312 m^3/s, 470 m^3/s, 770 m^3/s, and 1090 m^3/s, corresponding respectively to return periods of 10 years, 20 years, 50 years, and 100 years, respectively.

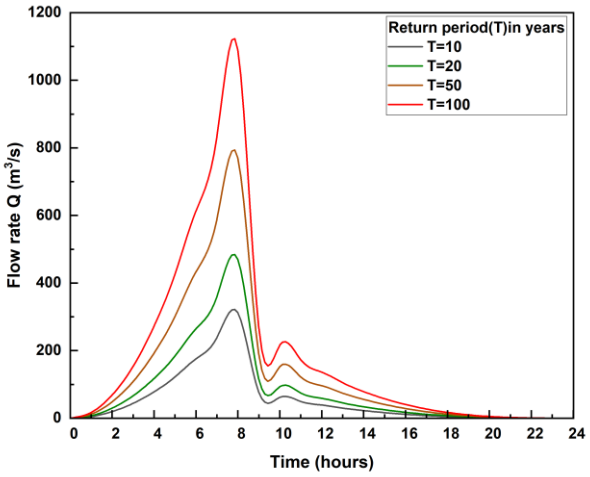

Figure 7. Flood hydrographs at the hydrometric station of Sidi Akkacha for different return periods: 10 years, 20 years, 50 years, and 100 years.

4.2. Validation model results

Two hydraulic simulation models in HEC-RAS were created from two digital elevation models. The first was derived from a Pléiades tri-stereo image (DSM), and the other was from a 12-m resolution model. The models were calibrated with a 2017 flood event by varying the Manning roughness coefficient values and comparing the simulated water line with the observed one. Thus, the following table (Table 4) reports the comparison results between the simulated and observed water lines. The results show a significant correlation between the simulated water line for the two topographic models and the observed water line, with coefficient of determination values of around 0.99 and 0.98 for the tri-stereo DSM and the DEM (12 m), respectively.

Table 4. Observed and simulated water level

Station (meters)	**3570**	**2860**	**1950**	**1450**	**750**	**350**	**150**
Observed water level (meters)	22.7	17.22	13.1	7.26	5.9	6.44	5.8
Simulated water level (DSM tri-stereo) (m)	22.06	16.03	9.98	7.81	6.34	4.85	2.85
Simulated water level (DEM 12 m) (m)	23.11	17.16	13.44	8.61	6.83	5.74	5.59
Determination coefficient R^2		**DSM (tri-stereo) 0.99**			**DEM (12 m) 0.98**		

4.3. Results of hydraulic simulation flood parameters

The simulation of different flood recurrence scenarios with the HEC-RAS model was allowed to extract the flood characteristics predicted for the two types of topographic models used upstream of the model. The most relevant parameters that can characterize and quantify the magnitude of the hazard are maximum water depths, flow velocities, the distribution of water surface elevations (WSE), and spatial flood boundaries.

Figures 8-10 show the maximum water depth, flow velocity, and WSE limits of simulated flooding as a function of the tri-stereo DSM and DEM models for the four return periods.

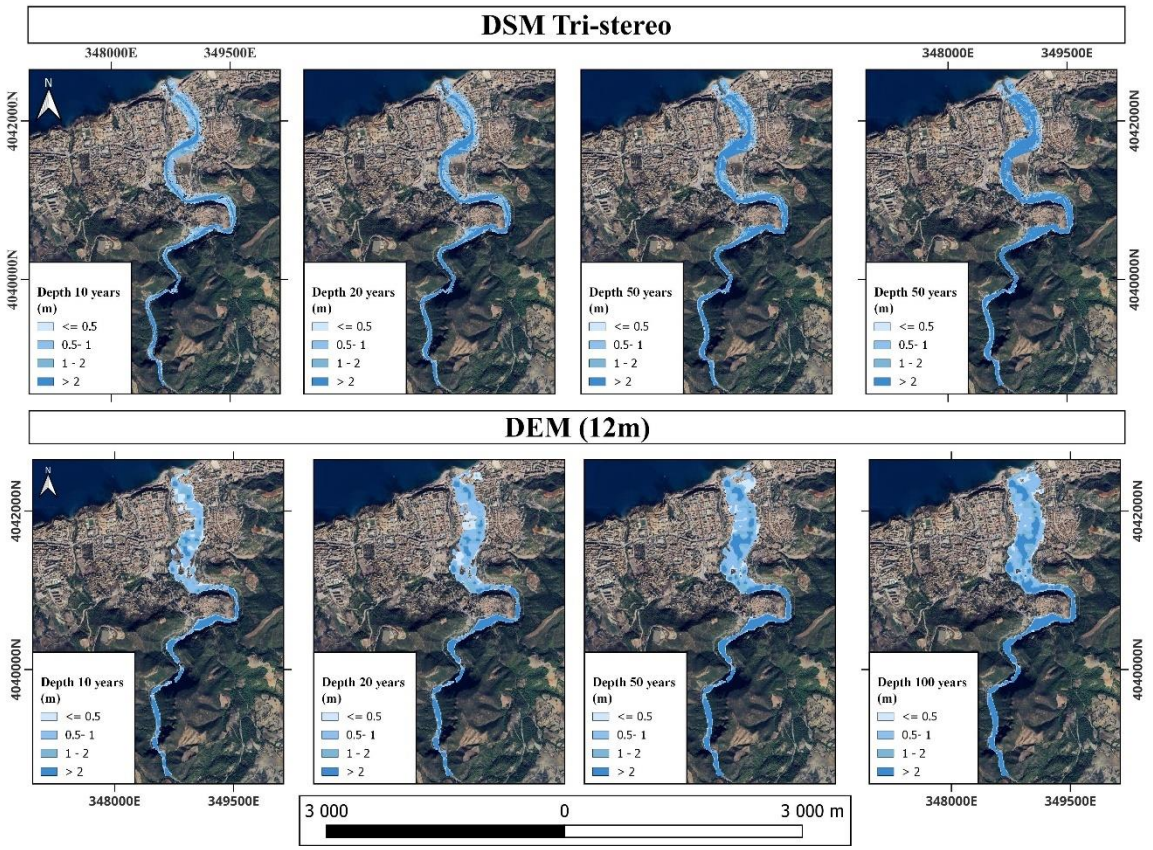

Figure 8. Water depths simulated by DSM tri-stereo and DEM for different return periods: 10 years, 20 years, 50 years, and 100 years.

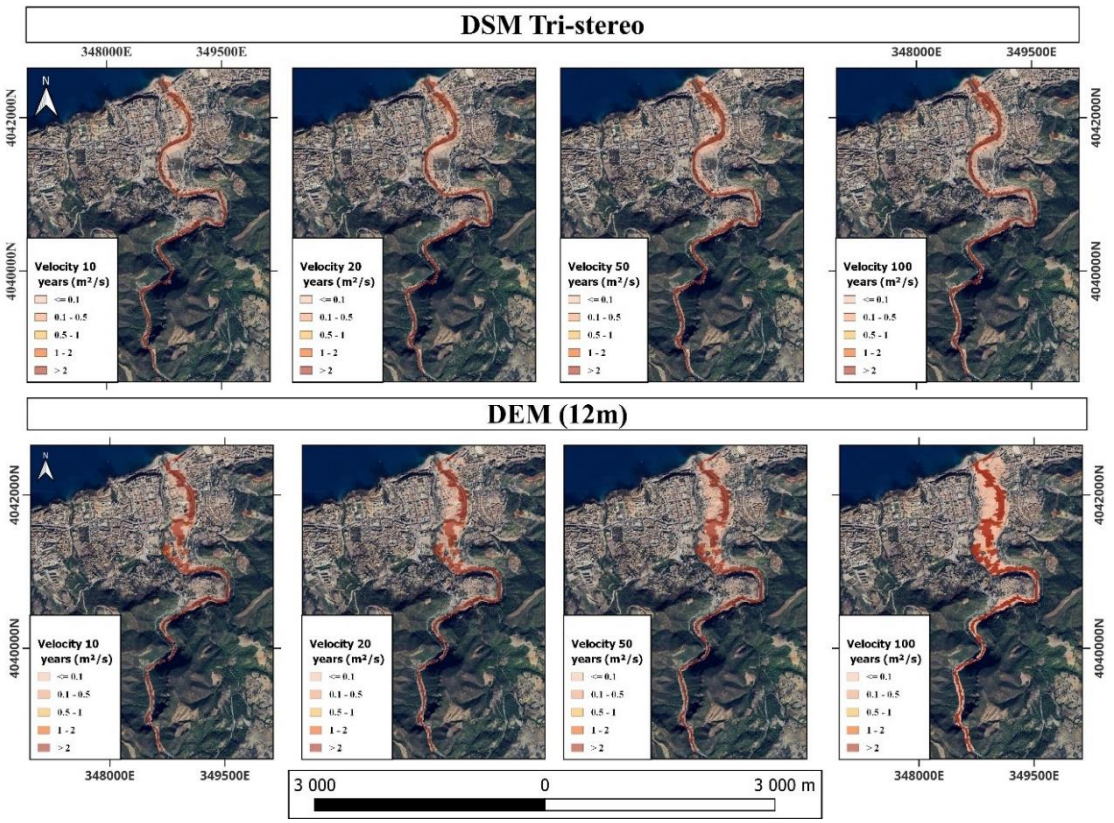

Figure 9: Simulated flow discharge velocity by DSM tri-stereo and DEM for different return periods: 10 years, 20 years, 50 years, and 100 years.

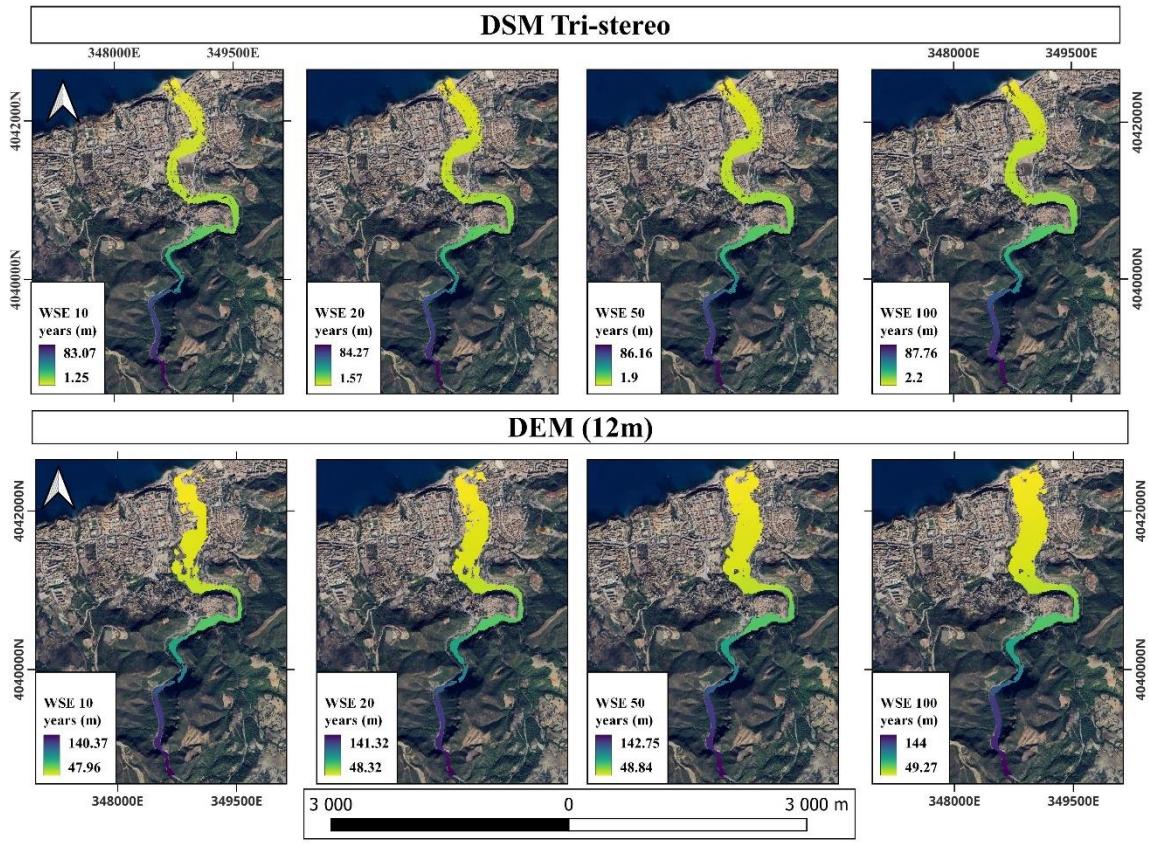

Figure 10. Simulated WSE by DSM tri-stereo and DEM for different return periods: 10 years, 20 years, 50 years, and 100 years.

A visual inspection of the maps produced by the two models confirms the statistical results of the simulations, where there are remarkable differences between the two simulation scenarios, particularly with respect to the spatial limits of inundation and the spatial fields of water depths. In fact, the tri-stereo DSM takes into account the surface elevations of infrastructure, buildings, bridges, and vegetation surfaces (such as medium vegetation and forests).

As a result, the geometry generated by this model was reasonable, and these topographical features appeared explicitly as flow obstacles in the final maps, especially in cases where their elevation is high (e.g., buildings or long trees). This is not the case for the DTM (12 m), which includes only natural terrain and no other surface features, including infrastructure, buildings, and bridges. Water depths increase from upstream to downstream, and the variations are different when comparing the main flow channel to the floodplain. The upstream portion (closest to the water level) is the most vulnerable to flooding due to the presence of buildings, structures, infrastructure, and roads.

Flow velocity is also an important parameter in describing simulated events. Considering the simulation results of the two terrain models, the simulation results of the flow velocity are shown in figure 9.

4.5. Flood hazard analysis

Flood risk analyses are performed for the two DSM tri-stereo and DEM (12 m) models used to build the simulation models. Hazard maps are generated based on water depths and flow velocities. Initially, and following the approach of Smith et al. (2014), six classes were identified. These classes were then reclassified into three classes to better represent the results according to three levels of risk (low-medium 0–0.6, medium, and high 0.6–1, and > 1). The flood risk maps for the four flood recurrence period scenarios generated by the HEC-RAS model are shown in Figures 11 and 12 for the DSM tri-stereo and DEM-12 m models.

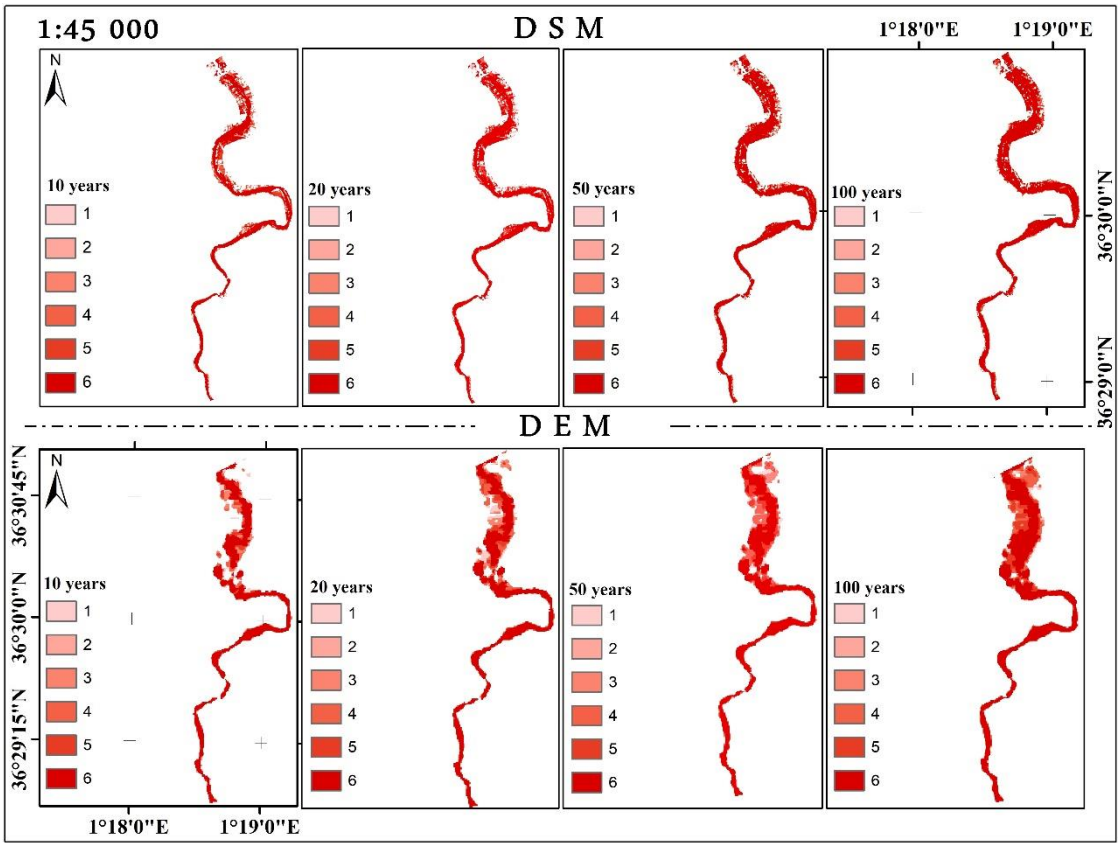

Figure 11. Simulated Flood hazard classes under 1D-HEC-RAS model for DSM and DEM models

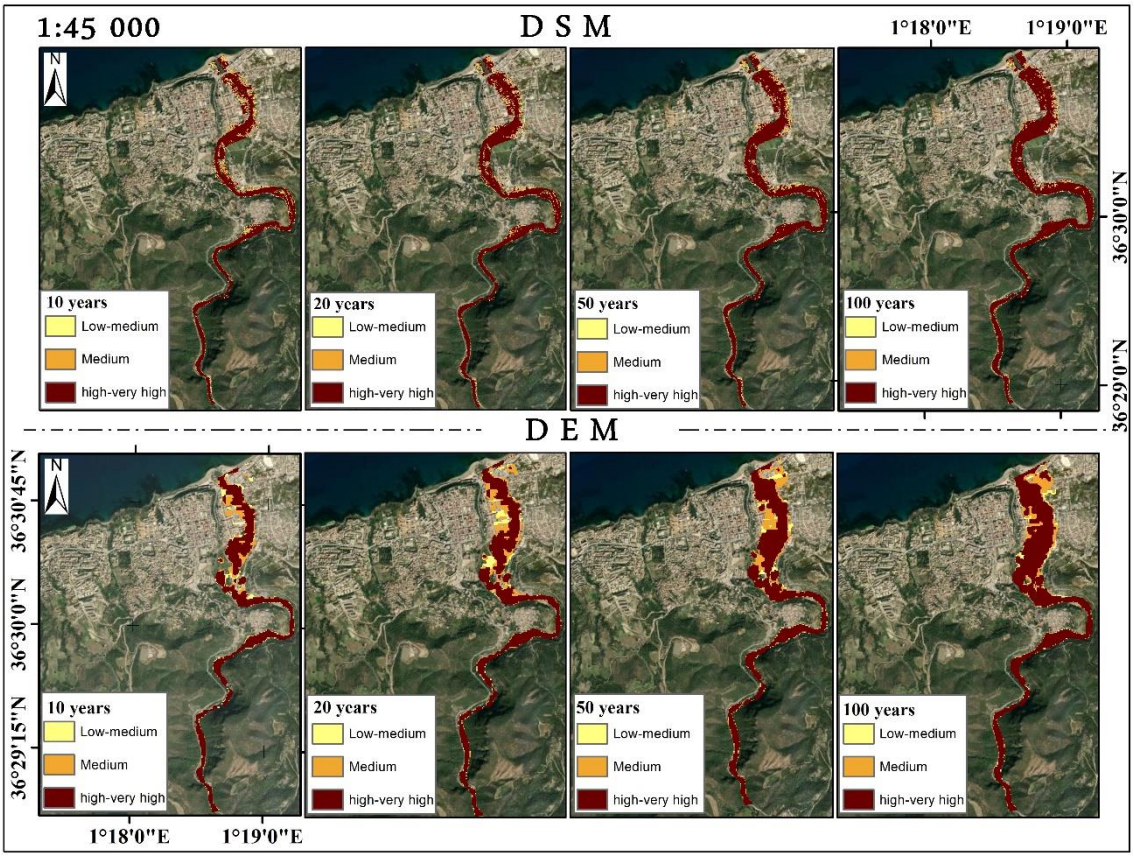

Figure 12. Produced Flood hazard maps for DSM tri-stereo and DEM models

The results of these maps show that potential flood areas are mainly located near rivers and extend into the floodplain of the Oued Allala catchment. Due to population growth, these areas are often characterized by infrastructure and construction. This urban concentration makes these areas the most critical and, therefore, the most vulnerable to flood risks. The results of this analysis are crucial for reducing and mitigating the impact of flood risks in different urban parcels of the study area's watershed.

4.6. Flood vulnerability analysis

Combining the hydraulic modeling results with the LULC maps allowed us to analyze and assess the exposure or vulnerability of the floodplain. The maps of flooded LULC classes and vulnerability according to these classes, generated from tri-stereo DSM and DEM (12 m), are shown in Figure 13.

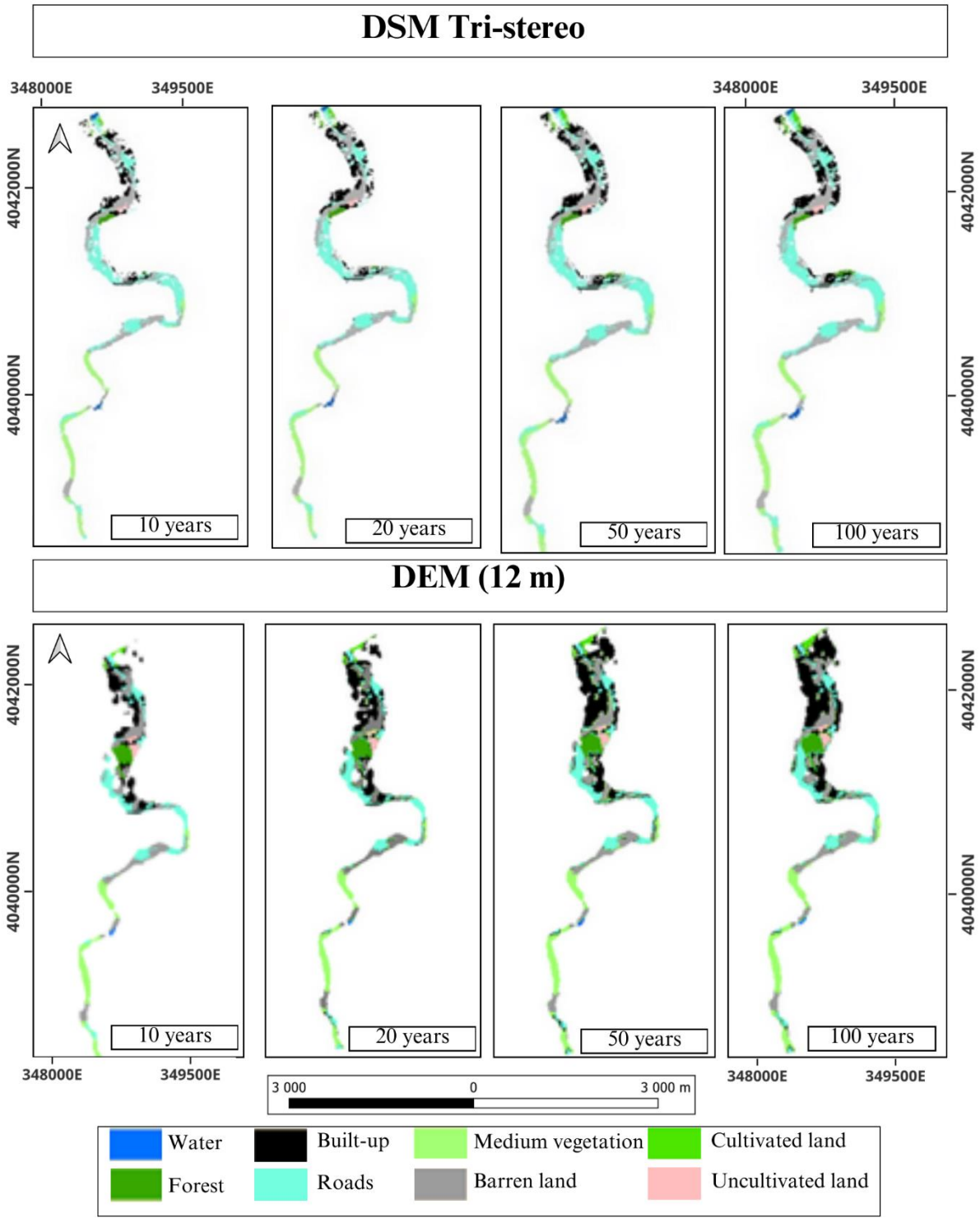

Figure 13. Flooded LULC classes using DSM and DEM models

With respect to the DSM tri-stereo simulation, the hydraulic analysis contributed to a total of 41.65, 45.42, 50.65, and 54.09 ha of flooded area in the study site, corresponding to return periods of 10 years, 20 years, 50 years, and 100 years, respectively.

The different LULC classes affected by flooding, including water, forest, buildings, roads, medium vegetation, cultivated land, barren land, and uncultivated land, are shown in Table 5 for the four return periods.

Table 5: Predicted flood zones (DSM tri-stereo) for different LULC types

Flooded areas (ha)	**LULC classes**								**Total (ha)**
	Water	Forest	Roads	Built-up	Medium vegetation	Barren land	Cultivated lands	Uncultivated lands	
10 years	0.47	0.73	14.59	6.85	5.78	12.38	0.41	0.44	41.65
20 years	0.5	0.8	15.66	7.87	6.15	13.43	0.56	0.45	45.42
50 years	0.57	1.02	17.07	9.16	6.9	14.64	0.82	0.47	50.65
100 years	0.69	1.25	17.79	9.96	7.68	15.31	0.91	0.5	54.09

For the 10-year return period, the classes (roads, buildings, and barren land) were the most at risk, with over 14.59 ha, 12.38 ha, and 6.85 ha, representing 35%, 29,7%, and 14.4% of the total flooded area, respectively. At the same time, for the 20-year return period, the same classes were the most affected by flooding, with over 15.66 ha and 13.43 ha, representing 34.47%, 29.7%, and 17.3% of the flooded area, respectively. This result means that the surface area of flooded buildings increases with an increasing return period. As for the 50-year scenario, similar to the 10-year and 20-year scenarios, roads, buildings, and bare soil were the classes most affected by flooding according to the simulated model, with 17.07 ha, 14.64 ha, and 9.16 ha of flooded area, respectively, representing 33.7%, 28.3%, and 18.1% of the total area affected by flooding. For the last scenario (100 years), more than 17.79 ha, 15.31 ha, and 9.96 ha of roads, bare ground, and buildings are flooded, representing 32.9%, 28.9%, and 18.4% of the total flooded area, respectively.

Therefore, the results showed that the longer the return period, the more vulnerable the plain is to flooding, and consequently, the flooded areas are larger in terms of surface area.

On the other hand, for the simulation with DTM (12 m), the hydraulic analysis contributed to a total of 51.81, 60.61, 70.40, and 76.40 ha of flooded area in the study site, corresponding to return periods of 10 years, 20 years, 50 years, and 100 years, respectively.

Table 6 shows the different LULC classes affected by flooding, including water, forest, buildings, roads, medium vegetation, cultivated land, barren land, and uncultivated land, for the four return periods.

For the 10-years return period, the classes (roads, buildings, and barren land) were the most at risk, with over 12.42 ha, 11.73 ha, and 14.60 ha, respectively. 24%, 22.6%, and 28.2% of the total flooded area, respectively. For the 20-years return period, the building class was the most affected by flooding, with over 16.20 ha, representing 26.7% of the flooded area.

This result shows that flooded construction has increased by 4.1% compared to the 10-year scenario. In the 50-years scenario, as in the 10-year and 20-year scenarios, the buildings and bare soil classes were the most affected by flooding according to the simulated model, with 21,38 ha and 17,35 ha of flooded areas, respectively, representing 30.4% and 24.6% of the total area affected by flooding, respectively. For the last scenario (100 years), more than 23.79 ha and 18.72 ha of buildings and bare ground, respectively, were flooded, representing 31.1% and 24.5% of the total flooded area. Similar to the DSM models, these results show that the longer the return period, the more vulnerable the plain is to flooding; consequently, the flooded areas are larger in terms of surface area.

Table 6: Predicted flood zones (DEM 12 m) for different types of LULC

Flooded areas (ha)	**Flooded land cover classes (ha)**								**Total (ha)**
	Water	Forest	Roads	Built-up	Medium vegetation	Barren land	Cultivated land	Uncultivated land	
10 years	0.20	3.17	12.42	11.73	7.62	14.60	0.69	1.38	51.81
20 years	0.22	3.69	14.20	16.20	8.17	15.69	0.95	1.49	60.61
50 years	0.25	3.88	15.56	21.38	9.21	17.35	1.21	1.56	70.40
100 years	0.29	1.25	16.58	23.79	9.98	18.72	1.47	1.59	76.40

Tables 7 and 8 show (for the DSM tri-stereo and DEM models) the LULC classes affected by flooding, broken down into the different flood risk classes, from medium-low to high-very-high, based on the criteria (Smith et al., 2014) for the different flood recurrence scenarios.

For the risk simulated by DSM tri-stereo, for all predicted return periods, the majority of flooded areas belong to the high-very-high (>1 m²/s) risk class with more than 35.36 ha, 40.28 ha, 45.92 ha, and 50.9 ha, corresponding to 84.91%, 89.82%, 90.6%, and 94.1% for 10-years, 20-years, 50-years, and 100-years return periods, respectively.

For the 10-years return period, over 71.5% (>1 m²/s) and 15.6% (0.6–1 m²/s) of roads and buildings are most vulnerable to flooding, accounting for over 49% of the total area. For the 20-year return period, over 89.82% of the class (>1 m²/s) and 12% of the class (0.6–1 m²/s), with over 48% and 65.6% of roads and buildings, respectively, are flooded. For the 50-years flood recurrence scenario, over 90.6% of the predicted flooded area is in the high and very high-risk zone (>1 m²/s), and 8.96% is in the medium-risk zone. For both risk classes, roads and buildings are considered to be the classes most affected by flooding, with over 51% and 56% of the total flooded area for the (>1 m²/s) and (0.6–1 m²/s) classes, respectively. Considering the last scenario (100 years), more than 94.1% of the flooded area is at high or very high risk (>1 m²/s), or 57.01% for roads and buildings. For the medium-risk class (0.6–1 m²/s), 4.65% of flooded areas are predicted, with a very high percentage of flooded roads and buildings (over 53.57%).

Table 7: Flood hazard risk based on areas in different LULC categories (DSM)

Hazard class		**Flooded land cover class (ha)**									**Total**
		Water	Forest	Roads	Built-up	Medium vegetation	Barren land	Cultivated land	Uncultivated land	Total/ risk class	
10 years	**< 0.6**	0.02	0.00	0.34	0.34	0.05	0.35	0.05	0.04	1.19	**41.65**
	0.6–1	0.15	0.09	2.15	1.20	0.19	1.19	0.11	0.02	5.1	
	>1	0.32	0.65	12.06	5.25	5.54	10.89	0.28	0.37	35.36	
20 years	**< 0.6**	0.00	0.03	0.37	0.45	0.03	0.13	0.06	0.00	1.07	**45.42**
	0.6–1	0.13	0.03	1.31	1.09	0.23	1.06	0.17	0.05	4.07	
	>1	0.40	0.76	13.96	6.24	5.86	12.26	0.39	0.41	40.28	
50 years	**< 0.6**	0.00	0.02	0.14	0.38	0.12	0.22	0.04	0.00	0.92	**50.65**
	0.6–1	0.03	0.17	1.02	1.13	0.50	0.74	0.21	0.01	3.81	
	>1	0.54	0.84	15.88	7.72	6.33	13.58	0.56	0.47	45.92	
100 years	**< 0.6**	0.00	0.00	0.13	0.22	0.11	0.19	0.02	0.00	0.67	**54.09**
	0.6–1	0.01	0.10	0.63	0.72	0.36	0.53	0.17	0.00	2.52	
	>1	0.68	1.14	16.96	9.06	7.25	14.56	0.74	0.51	50.9	

Table 8: Flood hazard risk based on areas of different LULC categories (DEM)

Hazard risk class		Flooded land cover class (ha)									Total (ha)
		Water	Forest	Roads	Built-Up	Medium vegetation	Barren land	Agricultural land	Non-agricultural land	Total/ risk class	
10 years	**< 0.6**	0.02	0.3	1.06	2.9	0.17	1.5	0.5	0.2	6.65	
	0.6–1	0	0.72	1.38	2.6	0.53	1.91	0.4	0.55	8.09	**51.81**
	>1	0.2	2.3	9.5	6	6.39	11.3	0.68	0.7	37.07	
20 years	**< 0.6**	0	0.41	1.17	4	0.22	0.52	0.2	0.04	6.56	
	0.6–1	0.05	1	2.25	6	0.6	3.1	0.2	1	14.2	**60.61**
	>1	0.2	2.45	10.21	6.4	7.74	11.6	0.55	0.7	39.85	
50 years	**< 0.6**	0	0.1	0.4	4.25	0.23	1.02	0.12	0	6.12	
	0.6–1	0.01	1.1	3.4	9.01	0.69	3	0.4	0.45	18.06	**70.4**
	>1	0.21	3.1	11.33	8.2	8.03	13.6	0.64	1.11	46.22	
100 years	**< 0.6**	0	0.1	0.59	2.31	0.09	0.99	0.12	0.02	4.22	
	0.6–1	0.01	0.82	2.7	11.97	0.73	2.49	0.45	0.12	19.29	**76.4**
	>1	0.27	3.3	12.87	9.92	8.52	15.75	0.8	1.46	52.89	

In addition, with regard to the predicted flood hazard classes (DEM 12 m; Table 10), for the first scenario (10-years return period), over 71.5% (>1 m²/s) and 15.6% (0.6–1 m²/s) of the roads and buildings are most vulnerable to flooding, with over 49% of the total surface area. For the 20-year return period, over 65.74% of the class (>1 m²/s) and 23.4% of the class (0.6–1 m²/s) had over 41.6% and 58% of the roads and buildings flooded, respectively.

For the 50-year flood recurrence scenario, over 65.6% of the predicted flooded area is in the high and very high-risk zone (>1 m²/s), and 25.6% is in the medium-risk zone. For both risk classes, roads and buildings are considered to be the classes most affected by flooding, with over 42.1% and 68.7% of the total flooded area for the (>1 m²/s) and (0.6–1 m²/s) classes, respectively. Considering the last scenario (100 years), more than 69.22% of the flooded areas are at high to very high risk (>1 m²/s), or 43.09% concern roads and buildings, and 29.77% bare flooded ground. For the medium-risk class (0.6–1 m²/s), more than 25.24% of flooded areas are predicted, with a very high percentage of flooded roads and buildings (more than 74%).

In summary, considering the criterion used to classify the flood risk according to the quantity depth x flow velocity, the high and very high-risk class has the highest percentage, with over

65% of flooded areas predicted by the 12 m DTM and over 73% by the tri-stereo DSM for all return periods. The road and construction classes (including infrastructure, buildings, single-family homes, and commercial spaces) represent the areas most affected by flooding in the majority of the proposed scenarios. The LULC vulnerability maps to flood risk for different return periods are shown in Figure 14.

This result shows that the northern plain of the Oued Allala watershed is, in fact, highly sensitive to the risk of very high levels of flooding, where there is a real danger to vehicles and people. Buildings are vulnerable to structural damage and are considered vulnerable to failure.

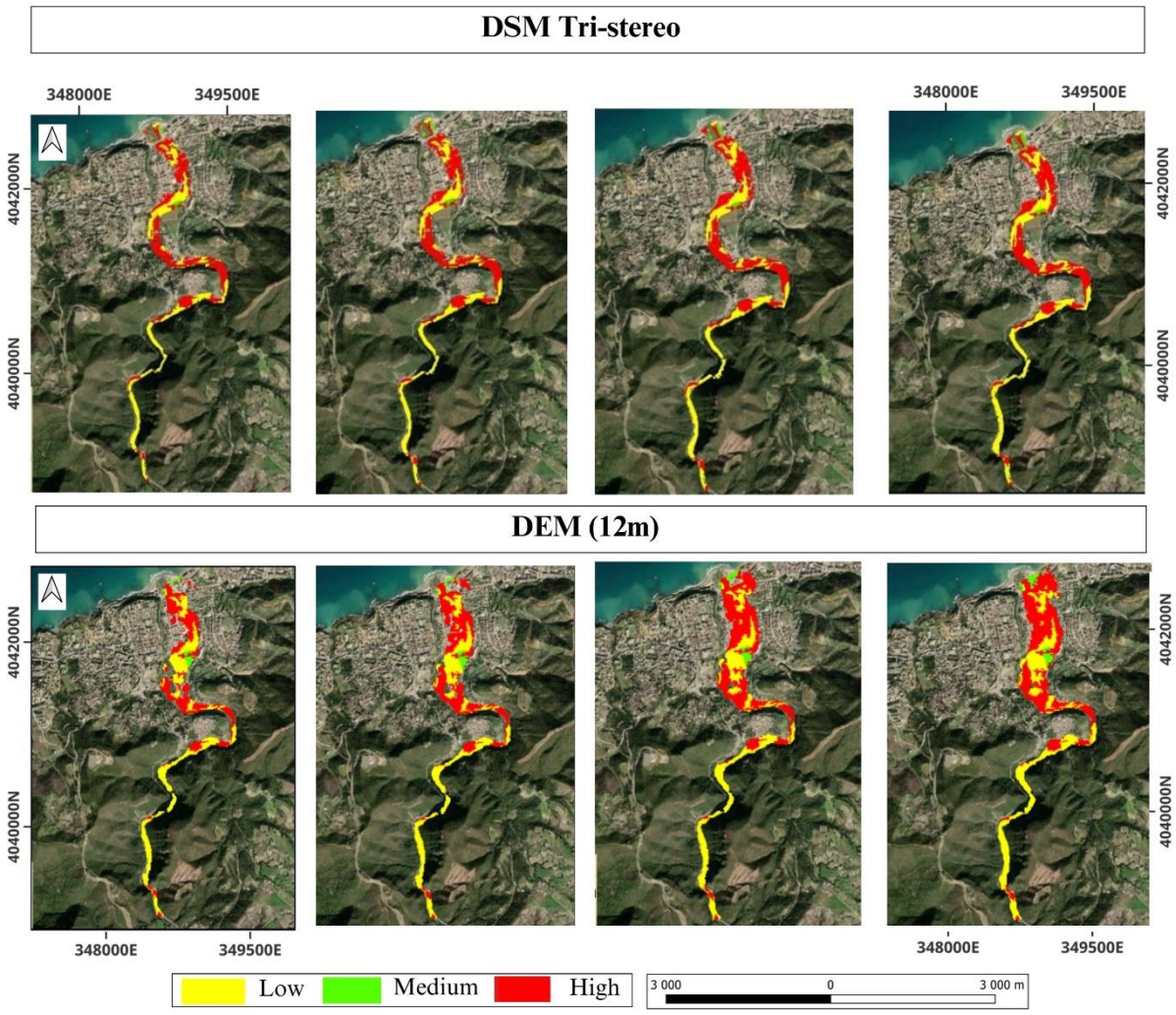

Figure 14. LULC vulnerability maps to flood risk for different return periods.

4.7. Overall risk analysis

Figure 15 shows the total risk maps generated by the DSM tri-stereo and DEM models. Table 9 shows the distribution of the total flood risk generated by the tri-stereo model in terms of surface area in hectares (ha). The risk increases with an increasing return period, and the degree of risk was medium to high. In terms of surface area, most of the areas at risk belong to the high-risk class, with more than 21.51, 23.52, 26.89, and 28.73 ha, respectively**.**

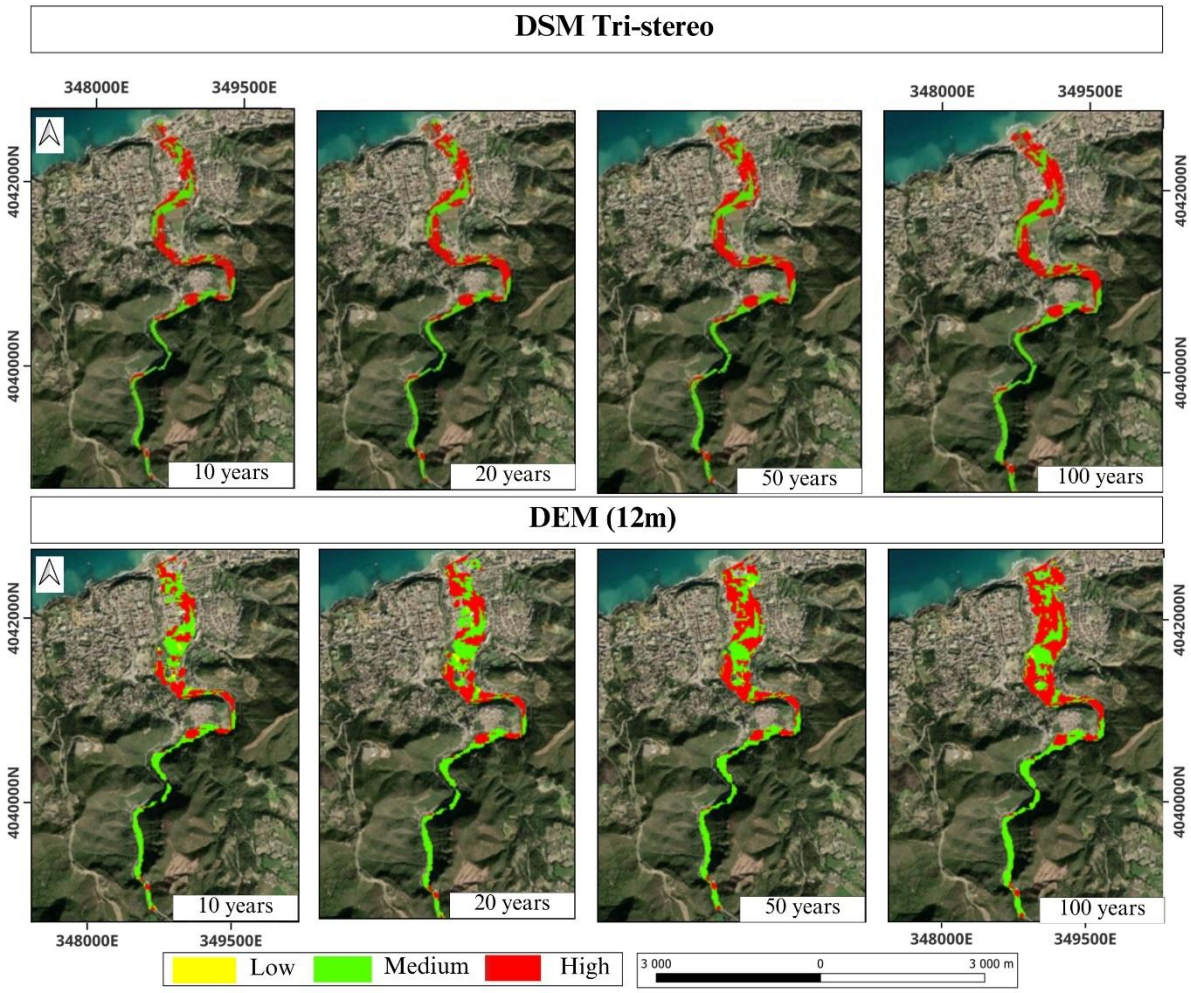

Figure 15. Global flood risk map for different return periods.

Table 9: Areas of the global risk classes with DSM (tri-stereo).

Risk	Area (ha)			
	10 years	20 years	50 years	100 years
Low	0.35	0.16	0.3	0.26
Medium	19.79	21.74	23.46	25.1
High	21.51	23.52	26.89	28.73
Total	41.65	45.42	50.65	54.09

Furthermore, Table 10 illustrates the distribution of the overall flood risk generated by the DEM model (12 m) in terms of surface area. The risk assessment trend increases with an increasing return period. For the first return periods (10 and 20 years), the degree of risk was more or less medium to high. For the 50- and 100-year return periods, in terms of surface area, most of the areas at risk belong to the high-risk class, with more than 34.8 ha for the 50-years return period and 39 ha for the 100-years return period.

Table 10: Areas of the global risk classes with DEM (12 m).

Risk	**Area (ha)**			
	10 years	20 years	50 years	100 years
Low	1.5	1.4	1.09	2.4
Medium	28	32.2	34.51	35
High	22.3	27	34.8	39
Total	51.8	60.6	70.4	76.4

Overall, for both simulation models, considering the most recent return periods, the risk of flooding is frequent in the Vieux-Ténès region, close to the coast, where infrastructures are at real risk. The overall risk is relatively high for the 50- and 100-years return periods, particularly on the right bank (from upstream to downstream) of the Oued Allala River (figure 14). From an operational point of view, the development of the Allala watercourse must be reinforced according to the results of the 100-years return period.

5. Discussion

In this work, we have tested a new approach to flood risk assessment based on the synergy of satellite data processing, combined with the different flood flow rates and the results of hydraulic simulations showing the flow for the different surface conditions of the urbanized environment. In terms of water depth, flow velocity, and flooded area, the 12 m DEM model predicted more severe flood scenarios than the DSM tri-stereo model. Remarkable differences were also observed in the flooded areas for all predicted return periods. In fact, the DEM (12 m) outperformed the tri-stereo DSM with more than 10.16 ha, 15.19 ha, 19.75 ha, and 22.31 ha of flooded areas for 10 years, 20 years, 50 years, and 100 years, respectively. These results explain why the predicted risk for the DTM (12 m) is higher than that of the tri-stereo DSM. This overestimation therefore implies an overestimation of the damage caused by the risk, particularly in terms of the zoning of land exposed to the risk of flooding. Figures 16 and 17 show examples of observed (2017 flood) and simulated (100-year) flow depths at some cross-section stations.

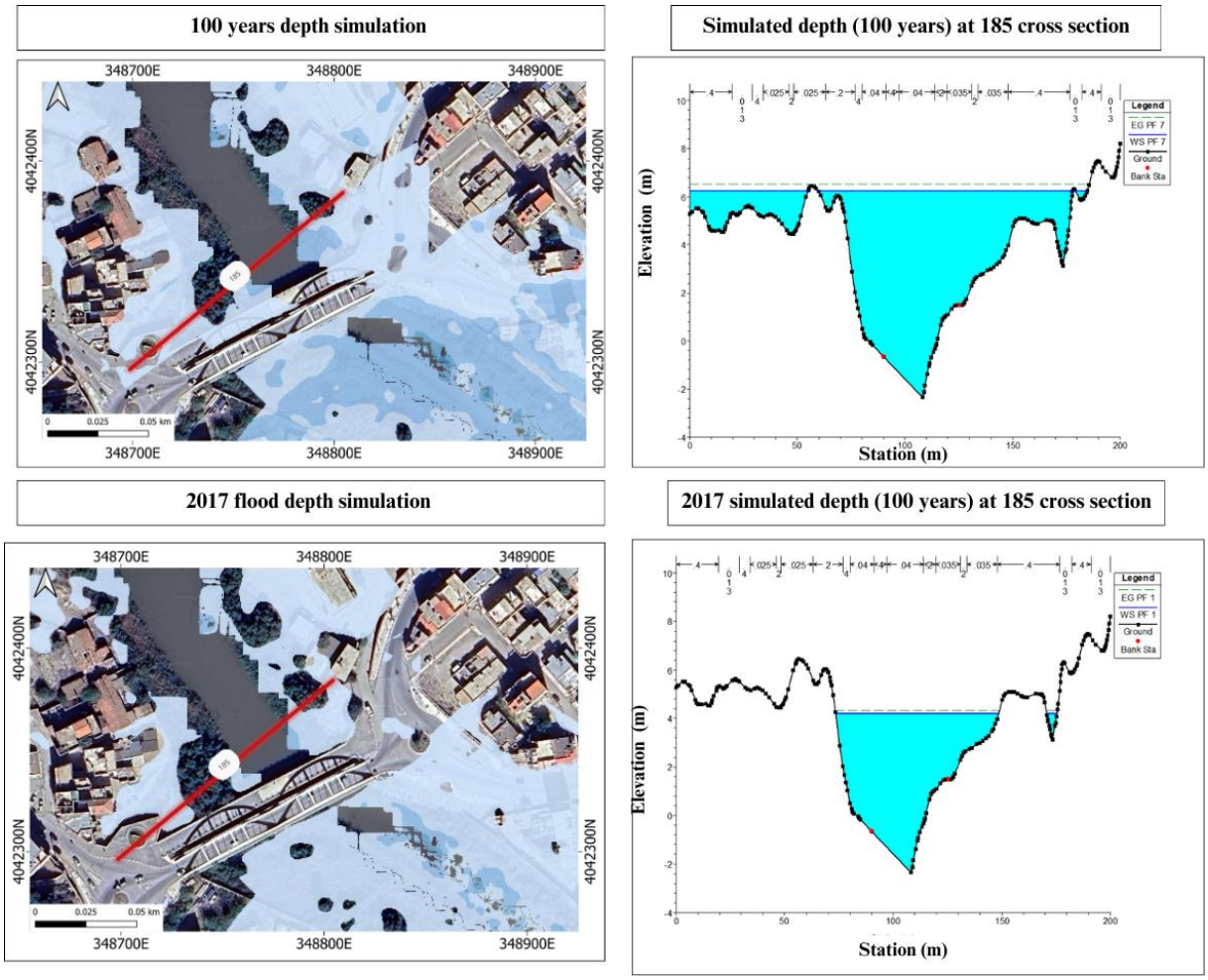

Figure 16. Observed (2017 flood) and simulated (100-year) flow depth at 185 m cross-station

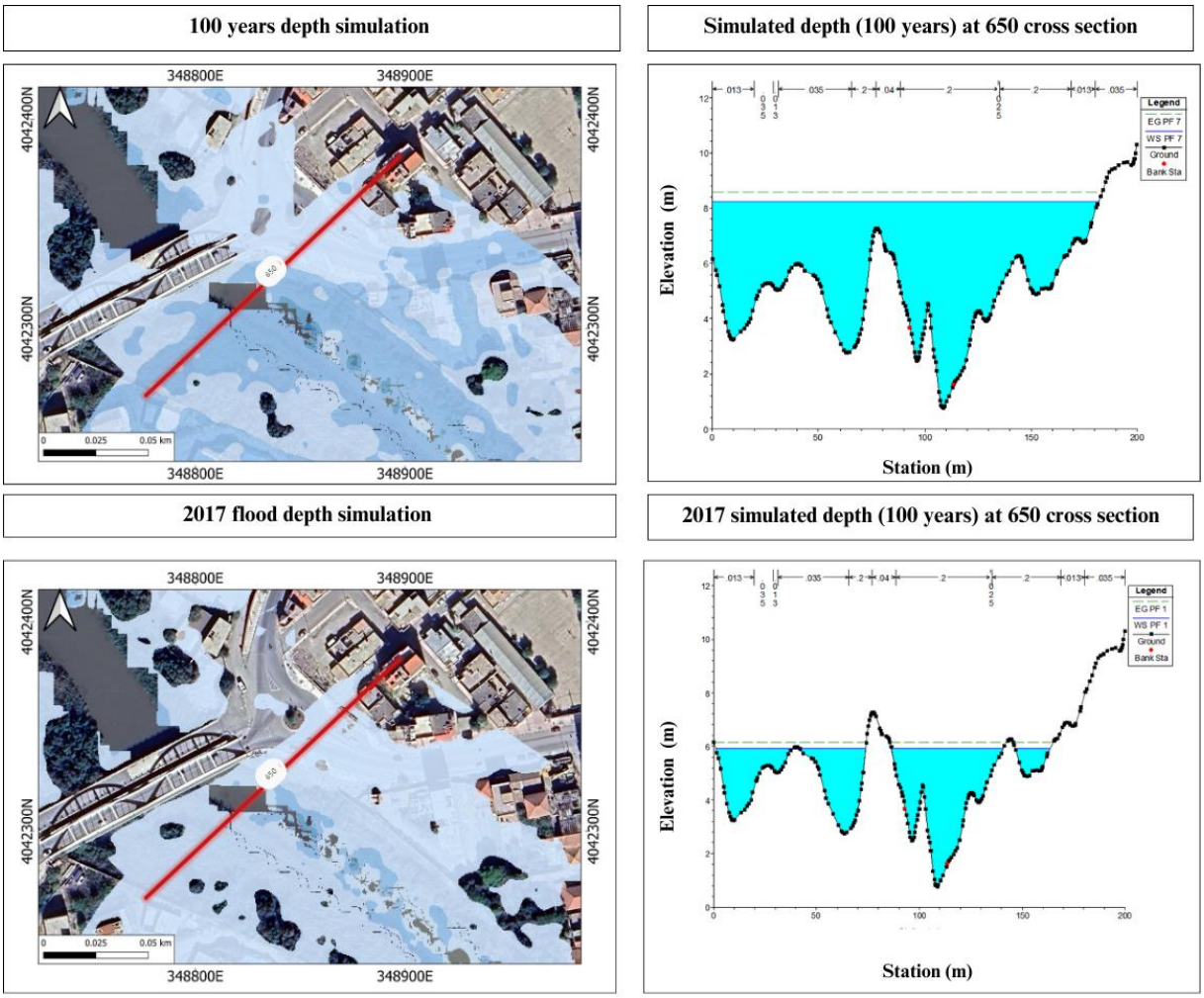

Figure 17. Observed (2017 flood) and simulated (100-year) flow depth at 650 m cross-station

Furthermore, in economic terms, if flood management in the affected area considers the results provided by the DEM (12 m), this means that even the cost of flood zone development and planning projects will be higher. Nevertheless, the predicted hazard risk is reasonable, and the simulation results are relatively consistent with those obtained by other applications in the same study area. For example, Kastali et al. (2021) assessed the flood risk in the Vieux-Ténès area under the effect of uncertainty in the rating curves. They used a field topographic model and performed simulations for the 100-year flood using HEC-RAS software. Considering the 100-year flow rate used for the simulation (1010 m^3/s), which is closest to the flow rate used in our case, the total flooded area was 58.30 ha. Compared to the results of our study (54.09 ha) simulated by DSM for the 100-year flood, we find a slight difference of 4 ha. As a result, this model proves to be reasonable and more reliable, providing a true estimate of the flooded area. The detailed flooded area function of the risk class is shown in Figure 18.

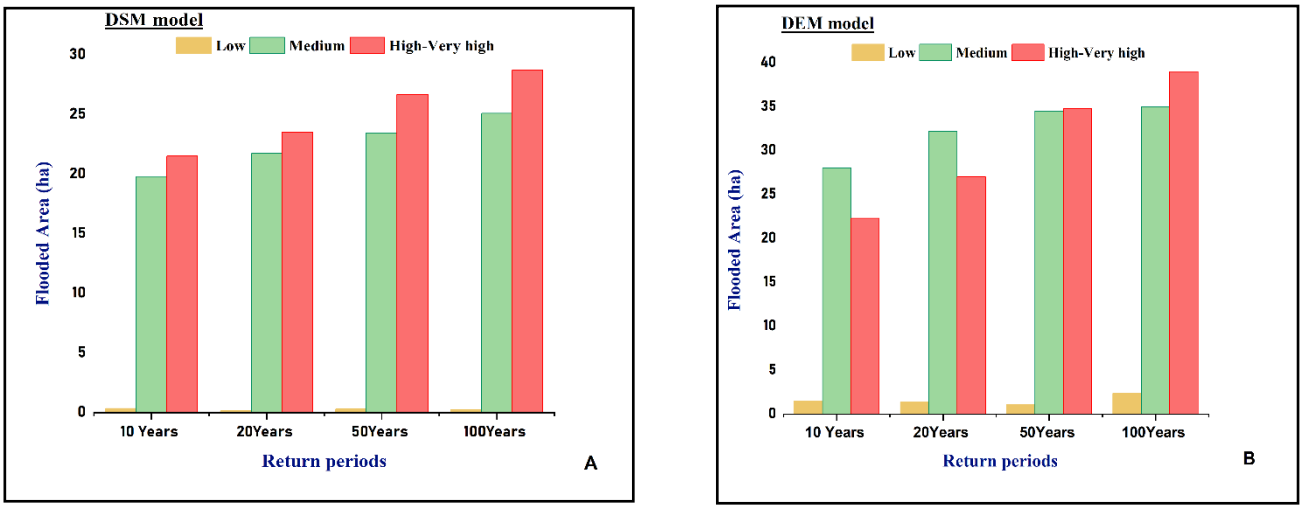

Figure 18. Flooded area for different return periods: A) DSM tri-stereo, B)DEM (12 m).

Figures 19–20 also give an overview of the results of the hazard risk analysis and the overall risk simulated by the 100-year return period.

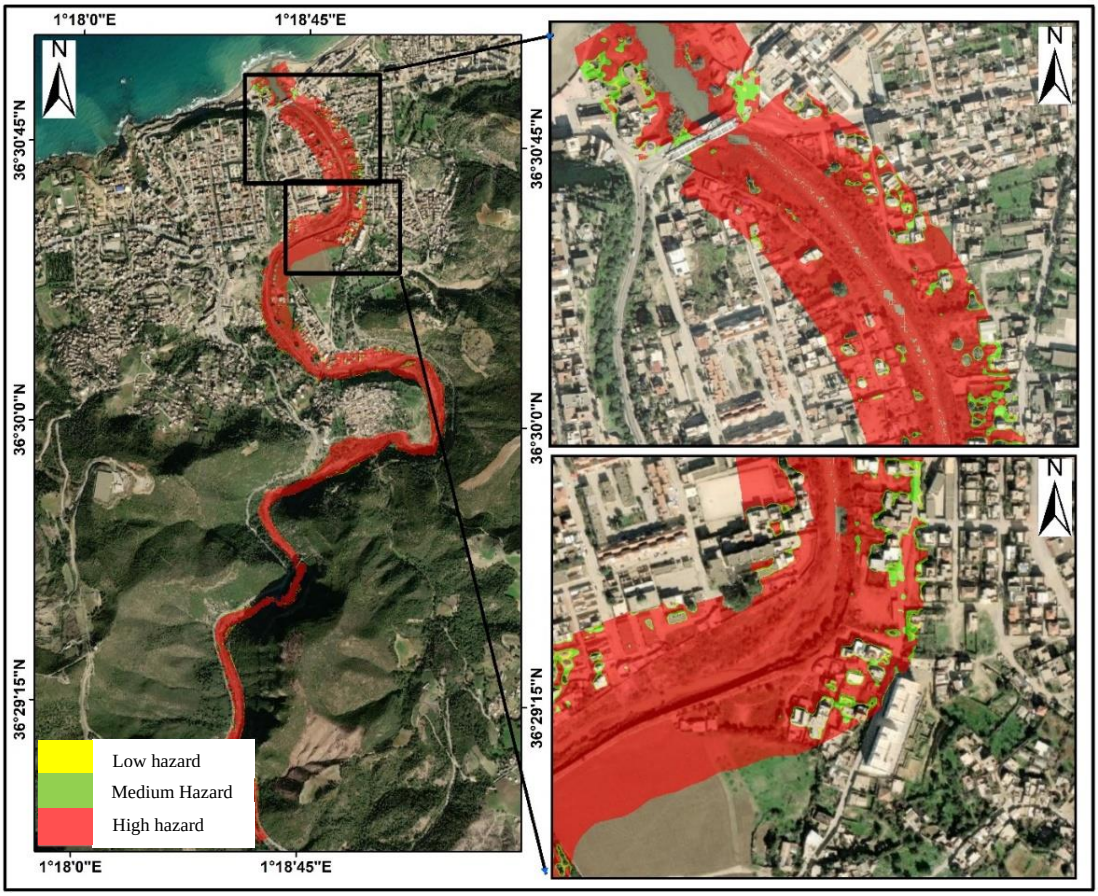

Figure 19. Zoom on the hazard risk simulated by the 100-year flood (DSM tri-stereo)

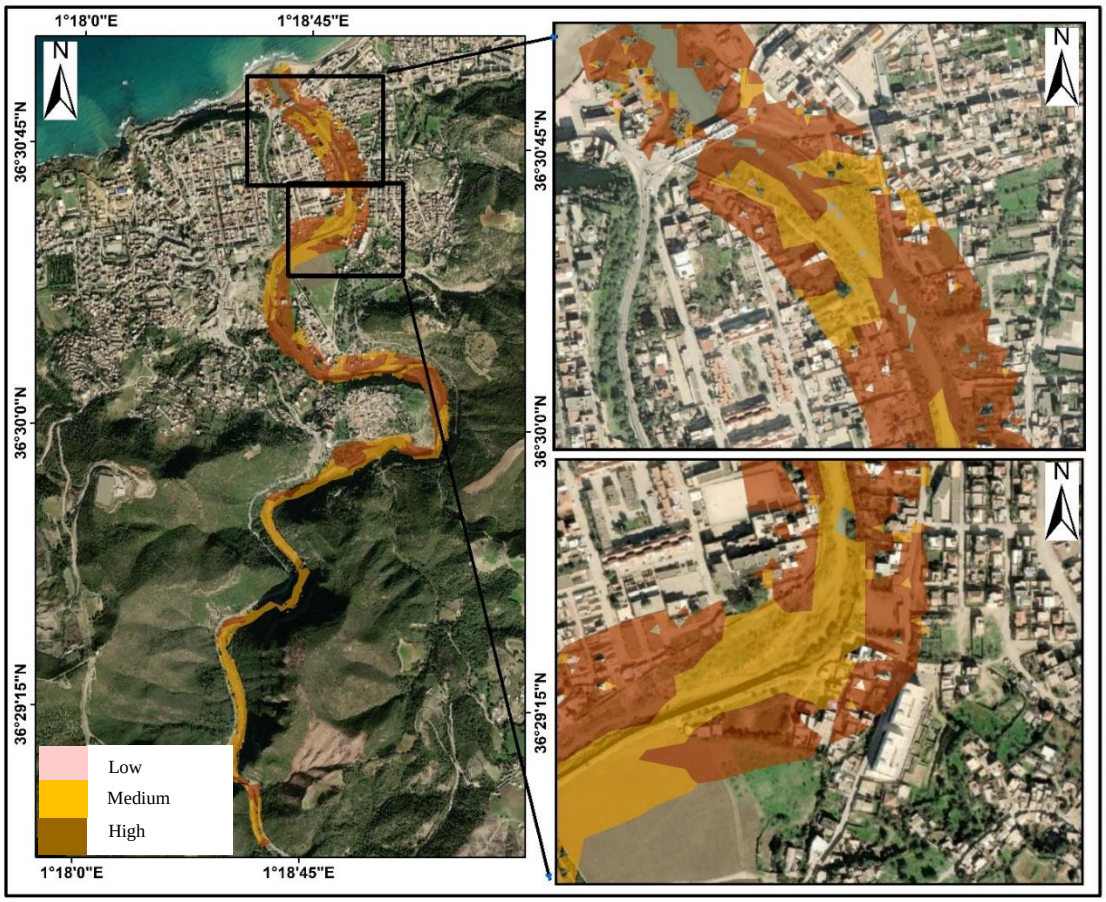

Figure.20. Zoom on the total flood risk simulated by the 100-year flood (MNS tri-stereo).

Although the very high spatial resolution satellite data used in this study contribute significantly to the effectiveness of such studies, they produce voluminous data that can require very demanding processing, revealing challenges and opportunities for many aspects of flood risk management systems. At the same time, the quality of the detailed information provided by the LULC classification perfectly contributed to the study of flooding in both aspects: hazard modeling and the vulnerability of flood-prone plains. This aspect has also been demonstrated in numerous studies (Zope et al., 2016; Sugianto et al., 2022).

A comparison of these results with other studies carried out in the same region demonstrated the reliability of the approach used; in particular, the results obtained using Pléiades tri-stereo data. Therefore, the powerful appearance of our study is the integration we have proposed between machine learning for LULC classification and hydraulic models. Other studies also use land use classification to build the same models, but they use less precise methods than machine learning. For example, in (Ahmad et al., 2023), the LULC map was obtained from ESRI's Land Cover website This database is available on a global scale based on ESRI methods of classification. In addition, the paper used a DEM with a spatial resolution less fine

than ours, which could influence the results, especially the LULC vulnerability maps. In similar, (Mohamed et al., 2023) used in their study one DEM model to assess the flood risk in the chosen study area. Regarding LULC, traditional methods integrated in GIS were used. Compared to the same studies, the main benefit of the study is the automatization of methods to conduct the proposed hydraulic model. For example, the Manning's roughness values generated from LULC classification, which represents a very important information in any flood simulation. In addition, with its potential for observing the Earth's surface and its tri-stereoscopic capability, Pléiades data offers the possibility of comprehensive flood risk mapping. The topographical data thus generated from the Pléiades data contributed to a relatively realistic simulation of flooding, considering all flow obstacles, especially in urban areas, and generating flows that were closer to reality. Obtained maps can serve as decision-support data on a national scale and the implementation of real crisis management measures, in particular with the modelling of small floods such as the 10-year flood. On a local scale, these maps could be as well integrated into the communal plans of security face to flood disasters.

Despite the advantages of the proposed synergistic method, which integrates advances in machine learning with land use and hydraulic modelling, there are a few limitations. Indeed, given the difficulty of accessing satellite data, images from active sensors are not used, which is one of the limitations of spatial representation of flood validation. Thus, other types of hydraulic models can be used for comparison with those developed under HEC RAS.

Conclusion

This study conducted a comprehensive analysis of flood risk, focusing on hazards and vulnerabilities within the Oued Allala watershed. Utilizing HEC-RAS software, flood scenarios were simulated across four return periods, leveraging land cover and land use (LULC) maps derived from the CNN deep learning model and OBIA classification, achieving an impressive accuracy exceeding 92%. The primary objective was to evaluate how remote sensing can enhance hydraulic simulation models. The methodology incorporated satellite imagery for LULC alongside high-resolution and topographic data, specifically from a Pléiades tri-stereo image and the ALOS satellite, to conduct the hydraulic model.

Hazard maps were generated based on simulated water depths and flow velocities, which were then correlated with LULC in flood-prone areas to assess vulnerability. This analysis identified specific LULC zones that could be affected by floods of varying return periods, ultimately leading to a comprehensive flood risk assessment. The findings revealed that flood-prone areas

are predominantly situated near the river and extend into the floodplain of the Oued Allala watershed, characterized by urban infrastructure and development. This urban concentration significantly heightens vulnerability to flooding.

The very high-resolution satellite data as well as machine and deep learning methods used in this work contribute significantly to the effectiveness of the constructed model. Indeed, the precision of the detailed information provided by the LULC classification contributes perfectly to the study of flooding in both aspects: hazard modeling and the vulnerability of flood-prone plains. This demonstrates CNN models' potential for image recognition and the delineation of flood-prone areas. Furthermore, the DSM created from Pléiades tri-stereo imagery offered a unique opportunity for accurate mapping of flood risk, enabling a realistic depiction of flood hazards while taking into consideration urban obstacles the same as vegetation and buildings.

Ultimately, the findings underscore that the coastal city of Ténès is acutely vulnerable to flood risks, necessitating immediate action to develop a flood risk prevention plan (PPRI) complemented by an early warning system at critical flow points and sections.

Acknowledgments

The authors would like to thank the CNES (Centre national d'études Spatiales) for the Pléiades images « Pléiades © CNES 2021, Distribution Airbus DS. » Cf. 2021-172 Sci P-001 This research was funded by the Hubert Curien (PHC)-Tassili project (19 MDU 207), the interdisciplinary graduate school for the blue planet (ISblue), and the program of ERASMUS+ Chair Jean Monnet European Spatial Studies of Sea and Coastal Zones (599967-EPP-1-2018-1-FR-EPPJMO-CHAIR).

References

Adugna, T., Xu, W., & Fan, J. (2022). Comparison of random forest and support vector machine classifiers for regional land cover mapping using coarse resolution FY-3C images. Remote Sensing, 14(3), 574.

Airbus, 2022, Pléiades Imagery User Guide. https://www.intelligence-airbusds.com/en/8718 user-guides.

Ahmad, I., Waseem, M., Ashraf, A., Leta, M.K., Ahmad, S., Wahab, H. (2023). Hydrological risk assessment for Mangla Dam: compound effects of instant flow and precipitation peaks under climate change, using HEC-RAS and HEC-GeoRAS.

Annis, A., Nardi, F., Petroselli, A., Apollonio, C., Arcangeletti, E., Tauro, F., ... & Grimaldi, S. (2020). UAV-DEMs for small-scale flood hazard mapping. Water, 12(6), 1717.

Bagnardi, M., González, P. J., & Hooper, A. (2016). High-resolution digital elevation model from tri-stereo Pleiades-1 satellite imagery for lava flow volume estimates at Fogo Volcano. Geophysical Research Letters, 43(12), 6267-6275.

Bhosle, K., & Musande, V. (2019). Evaluation of deep learning CNN model for land use land cover classification and crop identification using hyperspectral remote sensing images. Journal of the Indian Society of Remote Sensing, 47(11), 1949-1958.

Bourenane, H., Bouhadad, Y., & Guettouche, M. S. (2019). Flood hazard mapping in urban area using the hydrogeomorphological approach: case study of the Boumerzoug and Rhumel alluvial plains (Constantine city, NE Algeria). Journal of African Earth Sciences, 160, 103602.

Boutaghane, H., Boulmaiz, T., Lameche, E. K., Lefkir, A., Hasbaia, M., Abdelbaki, C., ... & Bermad, A. (2022). Flood analysis and mitigation strategies in Algeria. Wadi flash floods: challenges and advanced approaches for disaster risk reduction, 95-118.

Das, A., & Lindenschmidt, K. E. (2021). Evaluation of the sensitivity of hydraulic model parameters, boundary conditions and digital elevation models on ice-jam flood delineation. Cold Regions Science and Technology, 183, 103218.

Domeneghetti, A., Schumann, G. J. P., & Tarpanelli, A. (2019). Preface: remote sensing for flood mapping and monitoring of flood dynamics. Remote Sensing, 11(8), 943.

Dou, P., Huang, C., Han, W., Hou, J., Zhang, Y., & Gu, J. (2024). Remote sensing image classification using an ensemble framework without multiple classifiers. ISPRS Journal of Photogrammetry and Remote Sensing, 208, 190-209.

Dou, P., Shen, H., Huang, C., Li, Z., Mao, Y., & Li, X. (2024). Large-scale land use/land cover extraction from Landsat imagery using feature relationships matrix based deep-shallow learning. International Journal of Applied Earth Observation and Geoinformation, 129, 103866.

Casas, A., Benito, G., Thorndycraft, V. R., & Rico, M. (2006). The topographic data source of digital terrain models as a key element in the accuracy of hydraulic flood modelling. Earth Surface Processes and Landforms: The Journal of the British Geomorphological Research Group, 31(4), 444-456.

ECognition, 2021. [On line]. https://fr.geospatial.trimble.com/products-and-solutions/ecognition

Ettritch, G., Hardy, A., Bojang, L., Cross, D., Bunting, P., & Brewer, P. (2018). Enhancing digital elevation models for hydraulic modelling using flood frequency detection. Remote sensing of environment, 217, 506-522.

Fathy, I., Abd-Elhamid, H., Zelenakova, M., & Kaposztasova, D. (2019). Effect of topographic data accuracy on watershed management. International Journal of Environmental Research and Public Health, 16(21), 4245.

Garcia, M., & Liu, Y. (2022). Hydraulic Modeling for Flood Risk Assessment: A Case Study in Urban Areas. Water, 14(5), 678.

Goumrasa, A., Guendouz, M., Guettouche, M. S., & Belaroui, A. (2021). Flood hazard susceptibility assessment in Chiffa wadi watershed and along the first section of Algeria North–South highway using GIS and AHP method. Applied Geomatics, 13(4), 565-585.

Kastali, A., Zeroual, A., Remaoun, M., Serrano-Notivoli, R., & Moramarco, T. (2021). Design flood and flood-prone areas under rating curve uncertainty: area of Vieux-Ténès, Algeria. Journal of Hydrologic Engineering, 26(3), 05020054.

Kattenborn, T., Leitloff, J., Schiefer, F., & Hinz, S. (2021). Review on Convolutional Neural Networks (CNN) in vegetation remote sensing. ISPRS journal of photogrammetry and remote sensing, 173, 24-49.

Kosiorowski, D., Rydlewski, J. P., & Snarska, M. (2019). Detecting a structural change in functional time series using local Wilcoxon statistic. Statistical Papers, 60, 1677-1698.

Kreibich, H., Piroth, K., Seifert, I., Maiwald, H., Kunert, U., Schwarz, J., Merz, B., Thieken, A.H. (2009). Is flow velocity a significant parameter in flood damage modelling? Nat. Hazards Earth Syst. Sci. 9, 1679–1692. https://doi.org/10.5194/nhess-9-1679-2009.

Kumar, R., & Singh, P. (2024). Evaluating the Effectiveness of Flood Mitigation Strategies: A Hydraulic Perspective. Water Resources Research, 60(2), 234-250.

Lacroix, P., Berthier, E., & Maquerhua, E. T. (2015). Earthquake-driven acceleration of slow-moving landslides in the Colca valley, Peru, detected from Pléiades images. Remote Sensing of Environment, 165, 148-158.

Lamichhane, N., & Sharma, S. (2018). Effect of input data in hydraulic modeling for flood warning systems. Hydrological sciences journal, 63(6), 938-956.

Lu, T., Wan, L., Qi, S., Gao, M. (2023). Land Cover Classification of UAV Remote Sensing Based on Transformer–CNN Hybrid Architecture.

Luo, K., Lu, L., Xie, Y., Chen, F., Yin, F., & Li, Q. (2023). Crop type mapping in the central part of the North China Plain using Sentinel-2 time series and machine learning. Computers and Electronics in Agriculture, 205, 107577.

Mihu-Pintilie, A., Cîmpianu, C. I., Stoleriu, C. C., Pérez, M. N., & Paveluc, L. E. (2019). Using high-density LiDAR data and 2D streamflow hydraulic modeling to improve urban flood hazard maps: A HEC-RAS multi-scenario approach. Water, 11(9), 1832.

Mohamed, M.J., Karim, I.R., Fattah, M.Y., Al-Ansari, N. (2023). Modelling Flood Wave Propagation as a Result of Dam Piping Failure Using 2D-HEC-RAS. Civil Engineering Journal 9.

Mokhtari, E., Mezali, F., Abdelkebir, B., & Engel, B. (2023). Flood risk assessment using analytical hierarchy process: A case study from the Cheliff-Ghrib watershed, Algeria. Journal of Water and Climate Change, 14(3), 694-711.

Munawar, H. S., Hammad, A. W., & Waller, S. T. (2022). Remote sensing methods for flood prediction: A review. Sensors, 22(3), 960.

Nandam, Vineela et PATEL, P. L. (2021). A novel hybrid approach using SVM and spectral indices for enhanced land use land cover mapping of coastal urban plains. Geocarto International. 22 mars 2021. pp. 1-23. DOI 10.1080/10106049.2021.1899300.

Natarajan, S., & Radhakrishnan, N. (2020). An integrated hydrologic and hydraulic flood modeling study for a medium-sized ungauged urban catchment area: A case study of Tiruchirappalli City Using HEC-HMS and HEC-RAS. Journal of the Institution of Engineers (india): Series A, 101(2), 381-398.

Niculescu, S., Boissonnat, J. B., Lardeux, C., Roberts, D., Hanganu, J., Billey, A., ... & Doroftei, M. (2020). Synergy of high-resolution radar and optical images satellite for identification and mapping of wetland macrophytes on the Danube Delta. Remote Sensing, 12(14), 2188.

Nguyen, T., & Kim, H. (2023). Community-Based Approaches to Flood Risk Reduction in Vulnerable Areas. International Journal of Disaster Risk Reduction, 67, 102-115.

Psomiadis, E., Tomanis, L., Kavvadias, A., Soulis, K.X., Charizopoulos, N., Michas, S. (2021). Potential Dam Breach Analysis and Flood Wave Risk Assessment Using HEC-RAS and Remote Sensing Data: A Multicriteria Approach. Water 13, 364. https://doi.org/10.3390/w13030364.

Phyo, A.P. (2023). Managing dam breach and flood inundation by HEC-RAS modeling and GIS mapping for disaster risk management.

Schumann, G. J. P., & Moller, D. K. (2015). Microwave remote sensing of flood inundation. Physics and Chemistry of the Earth, Parts a/b/c, 83, 84-95.

SMITH, G P, DAVEY, E K et COX, R, [2014]. WRL Technical Report 2014/07. . pp. 59.

Smith, J., & Thompson, R. (2022). Integrated Flood Risk Management: Strategies for Planning in Flood-Prone Areas. Journal of Water Resources Planning and Management, 148(3), 04022001.

Solaimani, K., & Darvishi, S. (2024). Comparative analysis of land use changes modeling based-on new hybrid models and CA-Markov in the Urmia lake basin. Advances in Space Research, 74(8), 3749-3764.

Soliman, M., Morsy, M.M., Radwan, H.G. (2022). Assessment of Implementing Land Use/Land Cover LULC 2020-ESRI Global Maps in 2D Flood Modeling Application.

Sugianto, S., Deli, A., Miswar, E., Rusdi, M., Irham, M., 2022. The Effect of Land Use and Land Cover Changes on Flood Occurrence in Teunom Watershed, Aceh Jaya. Land 11, 1271. https://doi.org/10.3390/land11081271.

Tuia, D., Volpi, M., Copa, L., Kanevski, M., & Munoz-Mari, J. (2011). A survey of active learning algorithms for supervised remote sensing image classification. IEEE Journal of Selected Topics in Signal Processing, 5(3), 606-617.

Wald, A., & Wolfowitz, J. (1943). An exact test for randomness in the non-parametric case based on serial correlation. The Annals of Mathematical Statistics, 14(4), 378-388.

Wang, C., Chen, T., & Plaza, A., 2023. MFE-ResNet: A new extraction framework for land cover characterization in mining areas. Future Generation Computer Systems, 145, 550-562.

Wang, M., Zhang, X., Niu, X., Wang, F., & Zhang, X. (2019). Scene classification of high-resolution remotely sensed image based on ResNet. Journal of Geovisualization and Spatial Analysis, 3(2), 16.

Wang, L., Chen, Y., Tang, L., Fan, R., Yao, Y. (2018). Object-Based Convolutional Neural Networks for Cloud and Snow Detection in High-Resolution Multispectral Imagers. Water 10, 1666. https://doi.org/10.3390/w10111666.

Yalcin, E. (2020). Assessing the impact of topography and land cover data resolutions on two-dimensional HEC-RAS hydrodynamic model simulations for urban flood hazard analysis. Nat Hazards 101, 995–1017. https://doi.org/10.1007/s11069-020-03906-z.

Zaabar, N., Niculescu, S., & Mihoubi, M. K. (2021). Assessment of combining convolutional neural networks and object based image analysis to land cover classification using Sentinel 2 satellite imagery (Tenes region, Algeria). The International Archives of the Photogrammetry, Remote Sensing and Spatial Information Sciences, 43, 383-389.

Zaabar, N., Niculescu, S., & Kamel, M. M. (2022). Application of convolutional neural networks with object-based image analysis for land cover and land use mapping in coastal areas: A case study in Ain Témouchent, Algeria. IEEE Journal of Selected Topics in Applied Earth Observations and Remote Sensing, 15, 5177-5189.

Zhang, K., Gann, D., Ross, M., Robertson, Q., Sarmiento, J., Santana, S., ... & Fritz, C. (2019). Accuracy assessment of ASTER, SRTM, ALOS, and TDX DEMs for Hispaniola and implications for mapping vulnerability to coastal flooding. Remote sensing of Environment, 225, 290-306.

Zope, P.E., Eldho, T.I., Jothiprakash, V. (2016). Impacts of land use–land cover change and urbanization on flooding: A case study of Oshiwara River Basin in Mumbai, India. CATENA 145, 142–154. https://doi.org/10.1016/j.catena.2016.06.009.